

NeuPAN: Direct Point Robot Navigation with End-to-End Model-based Learning

Ruihua Han^{1,2}, Shuai Wang^{3,†}, Shuaijun Wang², Zeqing Zhang¹, Jianjun Chen², Shijie Lin¹,
Chengyang Li^{3,4}, Chengzhong Xu⁵, Yonina C. Eldar⁶, Qi Hao^{2,†}, Jia Pan^{1,†}

Abstract—Navigating a nonholonomic robot in a cluttered, unknown environment requires accurate perception and precise motion control for real-time collision avoidance. This paper presents NeuPAN: a real-time, highly accurate, map-free, easy-to-deploy, and environment-invariant robot motion planner. Leveraging a tightly coupled perception-to-control framework, NeuPAN has two key innovations compared to existing approaches: 1) it directly maps raw point cloud data to a latent distance feature space for collision-free motion generation, avoiding error propagation from the perception to control pipeline; 2) it is interpretable from an end-to-end model-based learning perspective. The crux of NeuPAN is solving an end-to-end mathematical model with numerous point-level constraints using a plug-and-play (PnP) proximal alternating-minimization network (PAN), incorporating neurons in the loop. This allows NeuPAN to generate real-time, physically interpretable motions. It seamlessly integrates data and knowledge engines, and its network parameters can be fine-tuned via backpropagation. We evaluate NeuPAN on a ground mobile robot, a wheel-legged robot, and an autonomous vehicle, in extensive simulated and real-world environments. Results demonstrate that NeuPAN outperforms existing baselines in terms of accuracy, efficiency, robustness, and generalization capabilities across various environments, including the cluttered sandbox, office, corridor, and parking lot. We show that NeuPAN works well in unknown and unstructured environments with arbitrarily shaped objects, transforming impassable paths into passable ones.

Index Terms—Direct point robot navigation, model-based learning, optimization based collision avoidance.

I. INTRODUCTION

Real-time navigation of robots in densely confined environments is crucial for a broad range of applications, including household robotics, logistics, and autonomous driving. In contrast to wide-open environments, the aforementioned cluttered scenarios require robot perceptions (i.e., providing necessary information about the environment) and motions (i.e., computing a sequence of feasible actions to connect the current and target states) to be very accurate under kinematic constraints; otherwise, efficiency or safety could be greatly

compromised. The situation becomes even more nontrivial if the navigation system needs to work properly in previously unseen environments.

Existing approaches fail to address the problem because of the following reasons: 1) Compressing a high-dimensional sensor space (e.g., massive points per second) into a low-dimensional action space (e.g., throttle and steer) while guaranteeing interpretability and preventing error propagation is nontrivial [1], [2]; 2) The navigation problem is PSPACE hard, and existing solutions [3]–[5] have to balance the trade-off between accuracy and complexity, resulting in either inexact motions, leading to conservative policies, or delayed motions, increasing the risk of collisions; 3) The solution should be stable, complete, and user-friendly, involving little hand-engineering and retraining for new robots and environments [6], [7]. The above system, algorithm, and engineering issues make dense-scenario navigation with only onboard computation resources a long-standing challenge.

To address these issues, this paper proposes NeuPAN, a direct point, end-to-end, model-based learning approach designed to achieve a real-time, highly accurate (e.g., over 2x improvement compared to state-of-the-art approaches), map-free, easy-to-deploy, and environment-invariant collision avoidance. Particularly, our solution employs lidar sensors to provide obstacle points because of their ability to deliver direct, active, and accurate depth measurements of environments, as well as their insensitivity to illumination variations and motion blur. Building upon these inherent features of lidar scans and empowered by NeuPAN, a wheel-legged robot can navigate through narrow gaps without a prior map while avoiding collisions with arbitrarily shaped dynamic objects, as demonstrated in Fig. 1.

The key contributions that lead to the superior performance of our system are as follows: 1) In contrast to existing approaches that convert point clouds to convex sets or occupancy grids, and adopt inexact minimum distances, NeuPAN directly processes massive raw points and computes the point flow based on predictive ego motion. Then a neural encoder is leveraged to map the point flow to a corresponding latent distance feature space, which represents the exact distance from the ego robot to the obstacle points within the receding horizon. 2) The latent distance features are seamlessly incorporated into the motion planner as a norm regularizer added to the loss function, accounting for the reward for departing from obstacles. The predictive states and actions generated by the motion planner are fed back to the front-end for re-computation of the point flow. This forms a tightly-coupled loop between per-

¹ Department of Computer Science, University of Hong Kong, Hong Kong, hanrh@connect.hku.hk

² Department of Computer Science and Engineering, Southern University of Science and Technology, Shenzhen, China

³ Shenzhen Institute of Advanced Technology, Chinese Academy of Sciences, Shenzhen, China

⁴ Robotics and Autonomous Systems Thrust, Hong Kong University of Science and Technology (Guangzhou), Guangzhou, China

⁵ IOTSC, University of Macau, Macau, China

⁶ Weizmann Institute of Science, Rehovot, Israel

[†] denotes the corresponding authors: Jia Pan (jpan@cs.hku.hk), Qi Hao (hao.q@sustech.edu.cn), Shuai Wang (s.wang@siat.ac.cn).

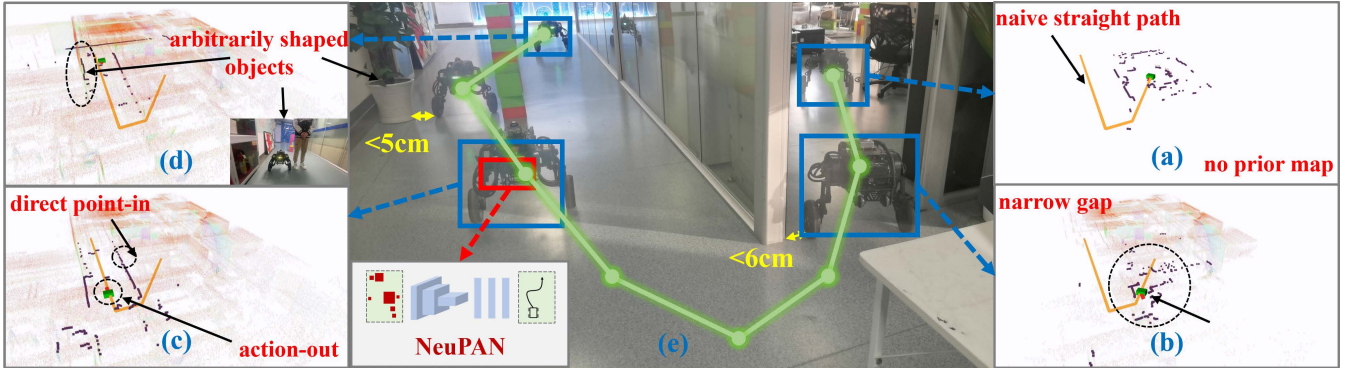


Fig. 1: Wheel-legged robot mapless navigation in the office empowered by NeuPAN: (a) the robot navigates along a naive path without a prior map; (b) the robot navigates through narrow gaps; ($< 6\text{cm}$); (c) NeuPAN utilizes a “direct point-in action-out” manner at a high frequency; (d) NeuPAN can handle arbitrarily shaped (moving) objects. (e) the robot trajectory.

ception and control. 3) To gain deeper insights into NeuPAN, we formulate an end-to-end mathematical program with point-level constraints. We demonstrate that NeuPAN is equivalent to solving this problem using the plug-and-play (PnP) proximal alternating-minimization (PAN) algorithm. To the best of our knowledge, this marks the first approach where a navigation algorithm is interpreted from a model-based learning perspective, thereby seamlessly integrating data-driven systems with rigorous mathematical models. 4) We conduct various experiments to evaluate the effectiveness of the developed NeuPAN system. Exhaustive benchmark comparisons in various simulated scenarios show that NeuPAN achieves consistently higher success rates with shorter navigation time than those of state-of-the-art robot navigation systems. We finally show the effectiveness of NeuPAN in real-world dynamic, cluttered, and unstructured environments including the sandbox, office, corridor, and parking lot on ground mobile robots, wheel-legged robots, and passenger autonomous vehicles. Experiment videos and more details can be found on our project page: https://hanruihua.github.io/neupan_project/.

The remainder of this paper is organized as follows. Section II reviews related work. Section III states the problem. Section IV describes the system architecture. Subsequently, Section V presents the neural encoder network and the neural regularized motion planner. Section VI presents simulation and real-world experiments. Finally, Section VII concludes this work.

II. RELATED WORK

A. Modular vs. End-to-End

Modular approaches, which divide navigation into distinct modules (e.g., an object detector and a motion planner in the simplest case), are the most widely adopted framework due to its reliability and ease of debugging [8]–[10]. However, these approaches suffer from error propagation from perception to control modules: 1) At the front-end perception layer, the detected object representation (e.g. bounding box) generated by even the best detector can deviate from the ground truth, necessitating the incorporation of a larger safety distance in the motion planner to guarantee worst-case collision avoidance; 2) At the intermediate representation layer, the box or convex sets

cannot exactly match real-world objects that may possess arbitrary nonconvex shapes; These errors in individual layers will add up together to the navigation pipeline, making the modular approach prone to getting stuck in cluttered environments.

To mitigate the error propagation inherent in the modular approach, recent robot navigation is experiencing a paradigm shift towards an end-to-end approach, which directly maps sensor inputs to motion outputs [7], [11], [12]. Earlier end-to-end solutions focused on using a single black-box deep neural network (DNN) to learn the mapping but were later found difficult to train and not generalizable to unseen situations. The emerging end-to-end approach adopts multiple blocks but differs from the modular approach in three aspects: 1) it exchanges features (e.g., encoder outputs) instead of explicit representations (e.g., bounding boxes) among modules; 2) the interaction among modules is bidirectional instead of unidirectional; 3) the entire system can be trained in an end-to-end manner. Such generalized end-to-end approaches have shown effectiveness in vision-based autonomous driving and encoder-based robot manipulation. For instance, the unified autonomous driving (UniAD) framework consists of backbone, perception, prediction, and planning modules, with task queries as interfaces connecting each node [13].

The majority of the industry practice has exploited end-to-end approaches for autonomous driving tasks, which leverage vision transformers to generate bird’s eye view (BEV) [14] for occupancy mapping [15] that is directly used for subsequent planning. Similar insights have been obtained for robot manipulation, which can be accomplished by a motion planning network (MPNet) consisting of a neural encoder and a motion planner [16]. The limitation of these purely data-driven techniques lies in their lack of interpretability. This makes it difficult to adjust the network parameters for new robot platforms. When generalizing to a new environment, they often require extensive hand-engineering and prolonged training and usually need to be accompanied by other conservative strategies to guarantee safety. These methods also demand significant data collection and annotation efforts.

B. Model-based vs. Learning-based

Algorithms determine the inference mapping of each module in modular or end-to-end frameworks. Existing algorithms can be categorized into model-based and learning-based.

Model-based algorithms utilize mathematical or statistical formulations that represent the underlying physics, prior information, and domain knowledge. Classical model-based algorithms include graph search-based, sampling-based, and optimization-based. Graph search-based techniques, e.g., A*, approximate the configuration space as a discrete grid space to search the path with minimum cost [17]. Sampling-based techniques, e.g., rapidly-exploring random tree (RRT) or RRT*, probe the configuration space with a sampling strategy [18]. The fast-likelihood-based collision avoidance method (Falco) [19], maximizes the likelihood to reach the goal in determining the next navigation actions. Optimization-based techniques generate trajectories through minimizing cost functions under dynamics and kinematic constraints [1], [9].

In the context of dense-scenario navigation, optimization-based techniques, such as model predictive control (MPC), are more attractive due to their ability to compute the current optimal input to produce the best possible behavior in the future, resulting in high-performance trajectories. One main drawback of optimization-based techniques is their high computational cost, which limits their real-time applications. Particularly, the number of collision avoidance constraints is proportional to the number of obstacles (spatial), and the length of the receding horizon (temporal). In cluttered environments, where the shape of obstacles is also taken into account, the computation time is further multiplied by the number of surfaces from each obstacle. To overcome the nonconvex collision avoidance constraints, the optimization-based collision avoidance (OBICA) algorithm is developed in [1] for full-shape control objects, which adopts duality to reformulate the exact distance based collision avoidance constraints. Moreover, full-shape robot navigation is further accelerated by a space-time decomposition algorithm in [20]. However, the frequency of these algorithms is not satisfactory when dealing with a dozen of objects. On the other hand, most existing works forgo exact distances and adopt inexact ones, such as center-point distances, approximate signed distances, or spatial-temporal corridors [21], [22]. Additionally, it is possible to convert hard constraints into soft regularizers for speed-up, as exemplified by the EGO planner, which removes the collision avoidance constraints by adding penalty terms [23]. While inexact algorithms achieve a high frequency (e.g., up to 100 Hz), they are not suitable for dense-scenario navigation, as discussed earlier in Section I.

In contrast to model-based approaches, learning algorithms dispense with analytical models by extracting features from data. This is particularly useful in complex systems where analytical models are not known. Consequently, learning algorithms are promising for end-to-end navigation tasks. In this direction, reinforcement learning (RL) is a major paradigm [26]. The idea of RL is to learn a neural network policy by interacting with the environment and maximizing cumulative action rewards [27]. In particular, RL has been widely

used for the dynamic collision avoidance (so-called CARL based approaches), where the motion information of obstacles is mapped to the robot actions directly, such as CADRL [28], LSTM-RL [29], SARL [6], RGL [30], and AEMCARL [24]. However, the performance of RL-based methods is influenced by the training dataset's distribution. Therefore, these methods are promising in simulation but often challenging to implement in real-world settings. Additionally, finding a suitable reward function for dense-scenario navigation is often difficult.

As mentioned in Section II-A, learning-based algorithms lack interpretability. Hence, an emerging paradigm involves the cross-fertilization of model-based and learning-based algorithms. This has led to a variety of model-based learning approaches in robot navigation. In particular, a direct way is to use learning algorithms to imitate complex dynamics or numerical procedures by transforming iterative computations into a feed-forward procedure. This is achieved by learning from solvers' demonstrations using DNNs. Examples include the neural PID in [31] and the neural MPC in [32]. On the other hand, learning-based algorithms are adopted to generate candidate trajectories, reducing the solution space for subsequent model-based algorithms, e.g., MPNet [16], MPC-MPNet [25], NFMPC [33], and MPPI [34]. Note that trajectory generation is often learned from classical sampling-based approaches. Lastly, learning algorithms can be used to adjust the hyperparameters involved in model-based algorithms. For instance, the cost and dynamics terms of MPC can be learned by differentiating parameters with respect to the policy function through the optimization problem [35], [36].

Our framework, NeuPAN, also belongs to the model-based learning approach. However, in contrast to the aforementioned works that are partially interpretable, NeuPAN is **end-to-end interpretable** from perception to control. This is achieved by solving an end-to-end optimization problem with numerous point-level constraints using the PnP PAN. This makes NeuPAN suitable for dense-scenario collision avoidance with nonholonomic robots, whereas existing results [7], [22], [23] usually consider holonomic drones or nonholonomic robots in wide-open scenarios. Similar to [35], [36], parameters within the costs and constraints of NeuPAN can be trained via function differentiation in an end-to-end fashion. Hence, NeuPAN enjoys easy-to-deploy and environment-invariant features.

C. Comprehensive Comparison with Existing Solutions

Comprehensive comparison with celebrated navigation approaches is provided in Table I. In particular, TEB [3], OBICA [1], RDA [20], STT [22], AEMCARL [24], and Falco [19] are modular approaches. Their inputs are grids, poses, boxes, or sets generated by a pre-established grid map or a front-end object detector. All these methods involve error propagation. In contrast to AEMCARL which treats the ego robot as a point (or ball), TEB, OBICA, RDA, STT, and Falco consider the shape of the ego robot and obstacles. However, TEB, STT, and Falco involve approximations when computing the distance. OBICA and RDA are the most accurate approaches but require high computational latency, e.g., up to second-level (i.e., less than 1 Hz). On the other hand, Hybrid-RL [7], MPC-MPNet [25], and NeuPAN (ours) are end-to-end

TABLE I: Characteristics comparison of NeuPAN and existing navigation approaches

Scheme	System Input	Full Shape	Exact distance	Map Free	Generalization	Latency [†]	Constraints Guarantee
TEB [3]	Grids	✓	✗	✗	✓	Low	✓
OBCA [1]	Object Sets	✓	✓	✗	✓	High	✓
RDA [20]	Object Sets	✓	✓	✓	✓	Medium~high	✓
STT [22]	Object Sets	✓	✗	✗	✓	Low	✗
AEMCARL [24]	Object Poses	✗	N/A	✓	✗	Low	✗
Hybrid-RL [7]	lidar scan	✗	N/A	✓	✗	Low	✗
MPC-MPNet [16], [25]	Voxel	✓	✗	✓	✗	Low	✓
Falco [19]	Voxel	✓	✗	✓	✓	Low	✓
NeuPAN (Ours)	Points	✓	✓	✓	✓	Low~Medium	✓

[†] low latency: < 50 ms; medium latency: 50 ~ 500 ms; high latency: > 500 ms.

approaches. By treating raw lidar points as inputs, these methods are free from error propagation. Hybrid-RL adopts a single network for point input and action output. Despite its high-level integration, Hybrid-RL suffers from poor generalization capability. MPC-MPNet, and NeuPAN adopt two networks, one for encoding and the other for planning: MPC-MPNet uses a neural encoder to map points into voxel features; NeuPAN uses a neural encoder to map points and predictive ego motions into latent distance features. All of them consider the shape of objects; however, due to the discretization from points to voxels, MPC-MPNet cannot compute the exact distances between two shapes. They also lack generalization as the trajectory generator is scenario-dependent and needs retraining for new robots. Our NeuPAN overcomes these drawbacks, at the cost of a slightly higher computational load.

NeuPAN is the first approach that builds the end-to-end mathematical model (i.e., point-in and action-out), and uses model-based learning to solve it. As such, NeuPAN is fully explainable. Owing to this new feature, NeuPAN generates very accurate, end-to-end, physically-interpretable motions in real time. This empowers autonomous systems to work in dense unstructured environments, which are previously considered impassable and not suitable for autonomous operations, triggering new applications such as cluttered-room housekeeper and limited-space parking. Compared to existing end-to-end methods, [7], [11]–[16], NeuPAN provides mathematical guarantee and leads to much lower uncertainty and higher generalization capability. Compared to existing model-based motion planning methods [1], [16], [20], [22], NeuPAN is more accurate, since conventional motion planning belongs to modular approaches and involves error propagation. There also exist other model-based learning methods [16], [31]–[34] for robot navigation. However, these methods are not end-to-end, e.g., [31], [32] consider state-in action-out, and [16], [33], [34] consider point-in trajectory-out. The work [25] considers point-in action-out, by bridging [16] with a back-end controller. However, such a bridge loses mathematical guarantee and no longer solve the inherent end-to-end model. The methods [16], [25] also leverage neural encoder like transformer to compress the sensor data, and this neural encoder has no interpretability.

III. PROBLEM STATEMENT

We consider an end-to-end navigation approach with points in and actions out for full-dimensional robots based on the model predictive control (MPC) framework. To reach the goal state through a control sequence, a perception-to-control optimization problem over a receding horizon $\mathcal{H} = \{t, \dots, t+H\}$ is solved iteratively at each time step t .

1) *Robot Kinematics*: Given the control vector \mathbf{u}_t , the current state \mathbf{s}_t and subsequent state \mathbf{s}_{t+1} should adhere to the discrete-time kinematic model:

$$\mathbf{s}_{t+1} = \mathbf{s}_t + f(\mathbf{s}_t, \mathbf{u}_t)\Delta t, \quad (1)$$

where Δt is the time slot between two states. We assume that the function $f(\mathbf{s}_t, \mathbf{u}_t)$ is linear with respect to the state \mathbf{s}_t and control vector \mathbf{u}_t . In scenarios involving non-linear dynamics, these functions can be approximated using linearization techniques, such as the Taylor series expansion. Accordingly, this constraint can be rewritten in a linear form:

$$\mathbf{s}_{t+1} = \mathbf{A}_t \mathbf{s}_t + \mathbf{B}_t \mathbf{u}_t + \mathbf{c}_t, \quad (2)$$

where $(\mathbf{A}_t, \mathbf{B}_t, \mathbf{c}_t)$ are coefficient matrices at time step t . Examples for ackermann and differential models are provided in Appendix A (Supplementary Material). Particularly, the state $\bar{\mathbf{s}}_t$ at initial time point under the MPC framework can be measured by odometry or provided by the localization system. Due to physical limits, the control vector \mathbf{u}_t should belong to a feasible control that set limits on the absolute values and rates of changes. This yields the following constraints:

$$\begin{aligned} \mathbf{u}_{\min} &\preceq \mathbf{u}_h \preceq \mathbf{u}_{\max}, \\ \mathbf{a}_{\min} &\preceq \mathbf{u}_{h+1} - \mathbf{u}_h \preceq \mathbf{a}_{\max}, \quad \forall h \in \mathcal{H}. \end{aligned} \quad (3)$$

Consequently, we define the kinematic feasible set \mathcal{F} as the set of all states and control vectors that satisfy the above constraints Eq. (2), (3)¹

2) *Robot Model*: The space occupied by the ego robot at the origin of the coordinate system can be represented by a compact convex set \mathbb{C} . Based on the conic inequality representation [37], \mathbb{C} is given by

$$\mathbb{C} = \{\mathbf{x} \in \mathbb{R}^n \mid \mathbf{G}\mathbf{x} \preceq_{\mathcal{K}} \mathbf{h}\}, \quad (4)$$

where, $\mathbf{G} \in \mathbb{R}^{l \times n}$ and $\mathbf{h} \in \mathbb{R}^l$ represent the rotations and translations of surfaces with respect to the zero point,

¹Note that $\mathbf{s}_t = \bar{\mathbf{s}}_t$, where $\bar{\mathbf{s}}_t$ is the current robot state in each horizon.

respectively, and l is the minimum number of surfaces that can represent the shape of ego robot. Symbol \mathcal{K} is a proper cone, with its partial ordering on \mathbb{R}^n defined as: $\mathbf{x} \preceq_{\mathcal{K}} \mathbf{y} \iff \mathbf{y} - \mathbf{x} \in \mathcal{K}$. For instance, for a polygonal robot, $\mathcal{K} = \mathbb{R}_+^n$ and l corresponds to the number of hyperplanes. Consequently, given the state \mathbf{s}_t , the occupied space at t -th time frame, denoted by the convex compact set \mathbb{Z}_t ²

$$\mathbb{Z}_t(\mathbf{s}_t) = \{\mathbf{R}_t(\mathbf{s}_t)\mathbf{x} + \mathbf{t}_t(\mathbf{s}_t)|\mathbf{x} \in \mathbb{C}\}, \quad (5)$$

where $\mathbf{R}_t(\mathbf{s}_t) \in \mathbb{R}^{n \times n}$ is the rotation matrix representing the orientation of the robot and $\mathbf{t}_t(\mathbf{s}_t) \in \mathbb{R}^n$ is the translation vector denoting the position of the robot. For instance, for a state in the 2D space with position and orientation angle $\mathbf{s}_t = [x_t, y_t, \theta_t]^T$, the rotation and translation matrices can be obtained by:

$$\mathbf{R}(\mathbf{s}_t) = \begin{bmatrix} \cos \theta_t & -\sin \theta_t \\ \sin \theta_t & \cos \theta_t \end{bmatrix}, \quad \mathbf{t}(\mathbf{s}_t) = \begin{bmatrix} x_t \\ y_t \end{bmatrix}. \quad (6)$$

3) *Point-Level Collision Avoidance Constraints*: We adopt a set of points to represent the obstacles in the environment at time t , denoted by $\mathbb{P}_t = \{\mathbf{p}_t^1, \dots, \mathbf{p}_t^i, \dots, \mathbf{p}_t^M\}$, where $\mathbf{p}_t^i \in \mathbb{R}^n$ is the n -dimensional position of the i -th point in the global coordinate system, and M is the total number of points. The set of obstacle points can be obtained directly from raw lidar scans in real-time. Therefore, conventional operations such as object detection or occupancy grid maps are not required. Consequently, the minimum distance between two non-intersecting sets, the robot $\mathbb{Z}_t(\mathbf{s}_t)$ and the t -th \mathbb{P}_t can be expressed as:

$$\begin{aligned} \text{dist}(\mathbb{Z}_t(\mathbf{s}_t), \mathbb{P}_t) &= \min_{\mathbf{e}} \{ \|\mathbf{e}\|_2 | (\mathbb{Z}_t(\mathbf{s}_t) + \mathbf{e}) \cap \mathbb{P}_t \neq \emptyset \} \\ &= \min\{D_{1,t}(\mathbb{Z}_t(\mathbf{s}_t), \mathbf{p}_t^1), \dots, D_{M,t}(\mathbb{Z}_t(\mathbf{s}_t), \mathbf{p}_t^M)\}, \end{aligned} \quad (7)$$

where \mathbf{e} denotes the smallest translation vector that brings these two sets into contact, as introduced in [1], [38]. $D_{i,t}(\mathbb{Z}_t(\mathbf{s}_t), \mathbf{p}_t^i)$ denotes the exact minimum distance between the point \mathbf{p}_t^i and the robot $\mathbb{Z}_t(\mathbf{s}_t)$.

The computation of distance $D_{i,t}$ is a convex optimization problem given by:

$$\begin{aligned} \min_{\mathbf{x}} \quad & \|\mathbf{R}_t(\mathbf{s}_t)\mathbf{x} + \mathbf{t}_t(\mathbf{s}_t) - \mathbf{p}_t^i\|_2^2 \\ \text{s.t.} \quad & \mathbf{G}\mathbf{x} \preceq_{\mathcal{K}} \mathbf{h}. \end{aligned} \quad (8)$$

We refer to the above convex optimization problem as the primal representation for computing the minimum distance. Accordingly, we have the point-level collision avoidance constraints:

$$\text{dist}(\mathbb{Z}_t(\mathbf{s}_t), \mathbb{P}_t) \geq d_{\min}, \quad (9)$$

where d_{\min} is a safety distance. Generally, these collision avoidance constraints are nonconvex and nondifferentiable [1].

4) *Objective Function*: Given the start state $\mathbf{s}_{\text{start}}$ and the goal state \mathbf{s}_{goal} , our objective is to find a control sequence $\mathcal{U} = \{\mathbf{u}_0, \dots, \mathbf{u}_T\}$ and associated trajectory $\mathcal{S} = \{\mathbf{s}_0, \dots, \mathbf{s}_T\}$, such that $\{\mathcal{S}, \mathcal{U}\} \in \mathcal{F}$, $\mathbf{s}_0 = \mathbf{s}_{\text{start}}$ and $\|\mathbf{s}_T - \mathbf{s}_{\text{goal}}\|_2 \leq \epsilon$, where ϵ is the navigation tolerance, while avoiding the obstacles in the environment. We adopt the naive straight line connecting

²Nonconvex objects can be represented as unions of convex objects.

$\mathbf{s}_{\text{start}}$ and \mathbf{s}_{goal} (same as [38]) as the initialization³, with a list of interpolating points $\{\mathbf{s}_0^\diamond, \mathbf{s}_1^\diamond, \dots\}$ on the line. In the case of multiple goal states, the initial path contains multiple line segments. A desired speed $\mathbf{u}_{\text{speed}}^\diamond$ is used as the initial value for the robot to maintain. In our case, the cost function $C_0(\mathcal{S}, \mathcal{U})$ is constructed as the distance between the output and naive trajectories over the horizon $\mathcal{H} = \{t, t+1, \dots, t+H\}$:

$$\begin{aligned} C_0(\mathcal{S}, \mathcal{U}) &= \sum_{h=t}^{t+H} \left(\|\mathbf{q}^\diamond(\mathbf{s}_{h+1} - \mathbf{s}_{h+1}^\diamond)\|_2^2 \right. \\ &\quad \left. + \|\mathbf{p}^\diamond(\mathbf{u}_{\text{speed},h} - \mathbf{u}_{\text{speed}}^\diamond)\|_2^2 \right), \end{aligned} \quad (10)$$

where $\{\mathbf{q}, \mathbf{p}\}$ are weighted parameters. A larger value of \mathbf{q} encourages the robot to follow the initialized trajectory more closely, while a larger value of \mathbf{p} control the robot to maintain the desired speed. $\{\mathbf{s}_{h+1}^\diamond, \forall h \in \mathcal{H}\}$ is selected from the naive path according to the closest distance criteria.

5) *Problem Formulation*: The direct point robot navigation problem is formulated as the following model predictive perception and control (MPPC) optimization problem over horizon \mathcal{H} :

$$\text{P} : \min_{\{\mathcal{S}, \mathcal{U}\} \in \mathcal{F}} C_0(\mathcal{S}, \mathcal{U}) \quad (11a)$$

$$\text{subject to} \quad \text{dist}(\mathbb{Z}_h(\mathbf{s}_h), \mathbb{P}_h) \geq d_{\min}, \forall h \in \mathcal{H}. \quad (11b)$$

Technical Challenge: P represents the direct point robot navigation problem. The input includes the point cloud \mathbb{P}_t , naive path $\{\mathbf{s}_0^\diamond, \mathbf{s}_1^\diamond, \dots\}$, and desired speed $\mathbf{u}_{\text{speed}}^\diamond$. The output is the optimized control vector and associated trajectory $\{\mathcal{S}, \mathcal{U}\}$. The collision avoidance constraints in P are bilevel, involving inner-level distance computations, and large-scale, as the number of point-level constraints, MH , can reach thousands. Existing model-based approaches convert \mathbb{P}_t to convex sets [1], [20], voxels [19], or grids [3] for constraint reduction. However, this would lead to degradation of solution accuracy.

IV. NEUPAN SYSTEM ARCHITECTURE

To keep the most accurate, complete, and dense information about the environments, we propose to directly process \mathbb{P}_t , resulting in an end-to-end perception-to-control approach for unstructured and unknown environments. The system architecture is illustrated in Fig. 2. Below, we first introduce the mathematical interpretation behind NeuPAN. Then we provide the detailed descriptions of the system.

A. Mathematical Interpretation

1) *Strong Duality Transformation*: To overcome the non-convexity and nondifferentiability of the collision avoidance constraints Eq. (9), we transform the exact minimum distance computation problem Eq. (8) to its dual problem under the strong duality property, as in [1], [20]:

$$\begin{aligned} D_t^i &= \max_{\lambda_t^i, \mu_t^i} \mu_t^{i\top} (\mathbf{G}\tilde{\mathbf{p}}_t^i(\mathbf{s}_t) - \mathbf{h}) \\ \text{s.t.} \quad & \mu_t^i \succeq_{\mathcal{K}^*} 0, \|\lambda_t^i\|_* \leq 1, \mu_t^{i\top} \mathbf{G} + \lambda_t^{i\top} \mathbf{R}(\mathbf{s}_t) = \mathbf{0}. \end{aligned} \quad (12)$$

³For Ackermann kinematics, Dubins or Reeds-Shepp paths can be adopted

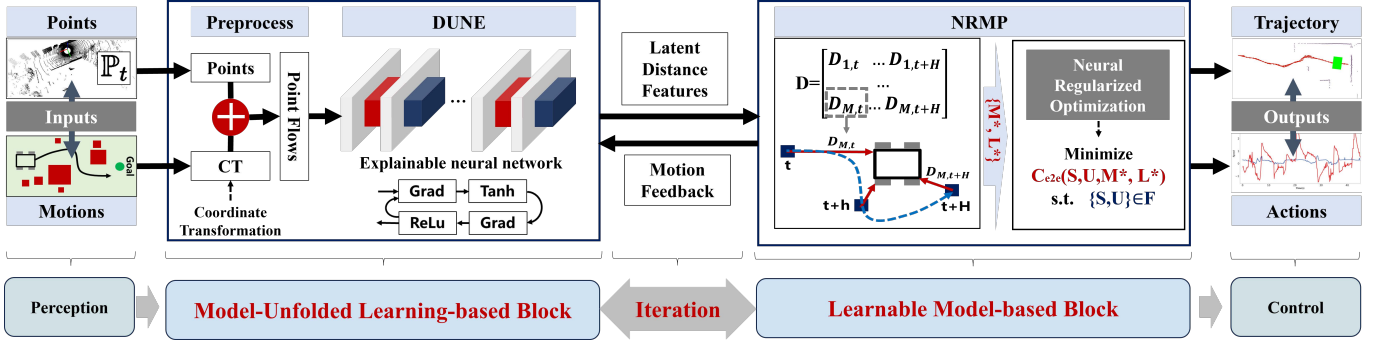


Fig. 2: System architecture of NeuPAN, a perception-to-control end-to-end approach for navigation, consists of two main blocks: learning-based and model-based.

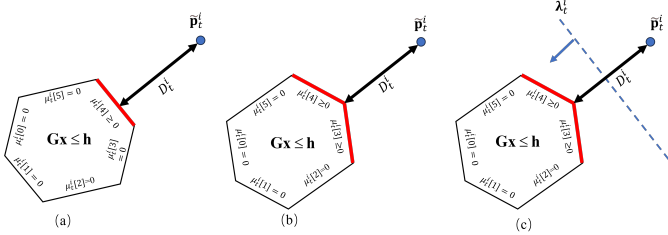


Fig. 3: Geometric interpretation of LDFs \mathcal{M} and \mathcal{L} . Red sides represent the closest robot edge(s) to the obstacle point. λ_t^i represents the normal vector of the separation hyperplane. Elements of μ_t^i with positive value represent the collision related red sides.

where \mathcal{K}^* represents the dual cone of \mathcal{K} , and $\|\cdot\|_*$ denotes the dual norm. $\tilde{\mathbf{p}}_t^i(s_t) = \mathbf{R}_t(s_t)^\top [\mathbf{p}_t^i - \mathbf{t}_t(s_t)]$ represents the position of the obstacle point in the ego robot coordinate system. $\mathcal{M} = \{\mu_t^i \in \mathbb{R}^l\}$ and $\mathcal{L} = \{\lambda_t^i \in \mathbb{R}^n\}$ are introduced as the Lagrange multipliers associated with the inequality and equality constraints respectively. Each point $\tilde{\mathbf{p}}_t^i$ is associated with a pair of μ_t^i and λ_t^i .

The geometric representation of \mathcal{M} and \mathcal{L} for a polygonal robot is shown in Fig. 3. It can be seen that the minimum distance D_t^i is determined by the obstacle point $\tilde{\mathbf{p}}_t^i$ and the closest edge(s) of the ego robot (depicted as one or two red sides in the figure). For μ_t^i , the elements corresponding to these red sides (related to collision) have positive values, while the other elements should be zero (unrelated to collision). For λ_t^i , it represents the normal vector of the separation hyperplane between the obstacle point $\tilde{\mathbf{p}}_t^i$ and the ego robot at time step t . Intuitively, (μ_t^i, λ_t^i) represent the matching and ranging from each obstacle point to its nearest robot edge. This representation sparsifies the distance computations by pruning unmatched edges for each obstacle point. Based on the above intuition, we define \mathcal{M} and \mathcal{L} as latent distance feature (LDF), and the set of all LDFs under the constraints in Eq. (12) can be denoted by $\{\mathcal{M}, \mathcal{L}\} \in \mathcal{G}$.

Leveraging the dual transformation and LDFs, we can reformulate the original problem P as an equivalent augmented dual form Q over $[\mathcal{S}, \mathcal{U}, \mathcal{M}, \mathcal{L}]$, which is a biconvex optimization

problem:

$$\text{Q} : \min_{\{\mathcal{S}, \mathcal{U}\} \in \mathcal{F}, \{\mathcal{M}, \mathcal{L}\} \in \mathcal{G}} \underbrace{C_0(\mathcal{S}, \mathcal{U}) + C_r(\mathcal{S}, \mathcal{M}, \mathcal{L})}_{:= C_{e2e}(\mathcal{S}, \mathcal{U}, \mathcal{M}, \mathcal{L})} \quad (13)$$

where

$$C_r(\mathcal{S}, \mathcal{M}, \mathcal{L}) = \frac{\rho_1}{2} \sum_{h=t}^{t+H} \sum_{i=0}^M \left\| \min(I(s_h, \mu_h^i, \lambda_h^i), 0) \right\|_2^2 + \frac{\rho_2}{2} \sum_{h=t}^{t+H} \sum_{i=0}^M \left\| E(s_h, \mu_h^i, \lambda_h^i) \right\|_2^2,$$

and ρ_1, ρ_2 are penalty parameters. The penalty functions I and E are

$$I(s_h, \mu_h^i, \lambda_h^i) = \lambda_h^i{}^\top (\mathbf{t}_h(s_h) - \mathbf{p}_t^i) - \mu_h^i{}^\top \mathbf{h} - d_{\min}, \quad (14)$$

$$E(s_h, \mu_h^i, \lambda_h^i) = \mu_h^i{}^\top \mathbf{G} + \lambda_h^i{}^\top \mathbf{R}(s_h). \quad (15)$$

As shown in Appendix B (Supplementary Material), the optimal solution to Q is also optimal to P. It can be seen that the bilevel collision avoidance constraints of P are transformed into biconvex distance costs. Intuitively, this transformation assigns a distance cost to these edge(s), which converts constraints into costs, facilitating subsequent problem decomposition.

2) *Problem Decomposition*: To facilitate the problem solving, Q is decomposed into two subproblems Q_1 and Q_2 :

- Q_1 : Involving variables \mathcal{M} and \mathcal{L} while keeping $\bar{\mathcal{S}}$ and $\bar{\mathcal{U}}$ fixed, detailed in Section V-A.
- Q_2 : Involving variables \mathcal{S} and \mathcal{U} while keeping $\bar{\mathcal{M}}$ and $\bar{\mathcal{L}}$ fixed, detailed in Section V-B.

These subproblems are solved alternately in each iteration. Specifically, as illustrated in Fig. 4, subproblem Q_1 is a motion aware model predictive perception (MAMPP) problem to generate $[\bar{\mathcal{M}}, \bar{\mathcal{L}}]$ for Q_2 . Subproblem Q_2 is a perception regularized model predictive control (PRMPC) problem to generate new $[\bar{\mathcal{S}}, \bar{\mathcal{U}}]$. This iterative process continues until convergence, yielding the final solution $[\mathcal{S}^*, \mathcal{U}^*]$. The convergence and complexity analysis of the proposed algorithm are provided in Section V-C. Intuitively, Q_1 encodes the point cloud and robot shape into LDFs $[\mathcal{M}, \mathcal{L}]$, which is a high-dimension but easy-to-unfold problem. Meanwhile, Q_2 maps the LDFs from Q_1 to robot action, which is a low-dimension

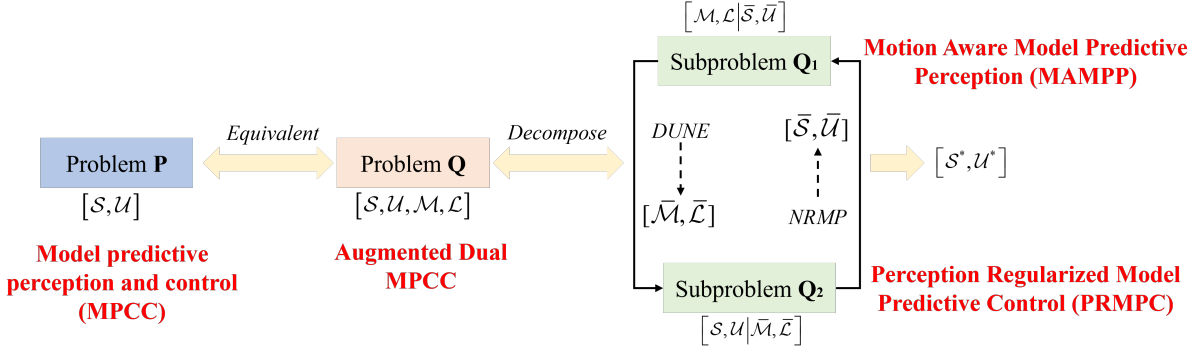


Fig. 4: Relationship between problems P, Q, Q₁, and Q₂

but complex optimization problem. This decomposition allows for efficient handling of the large number of direct point collision avoidance constraints by dividing the problem into more manageable components.

B. NeuPAN System

As shown in Fig. 2, in each MPPC horizon, NeuPAN transforms raw points to point flow $\widetilde{\mathbb{P}\mathbb{F}}$ by the preprocess block, incorporating the motion feedback, then to LDFs by the learning-based block addressing problem Q₁, and finally to robot control actions by the model-based block addressing Q₂. The solution (i.e., containing robot actions and associated trajectories) generated by the model-based block is fed back to the preprocess block for re-generation of point flow, which forms a tightly-coupled closed-loop between perception and control. Below we present the structure of each block.

1) Model-unfolded learning-based block: We first preprocess the inputs by transforming the coordinates of obstacle points \mathbb{P}_t , from the global coordinate system to the robot's local coordinate system within the MPPC receding horizon framework. Given a set of obstacle points $\mathbb{P}_t = \{\mathbf{p}_t^1, \dots, \mathbf{p}_t^M\}$ and their associated velocities $\mathbb{V}_t = \{\mathbf{v}_t^1, \dots, \mathbf{v}_t^M\}$ at time t , the point flow over the horizon H in the global coordinate system should be:

$$\mathbb{P}\mathbb{F}_t = \begin{bmatrix} \mathbf{p}_t^1 & \cdots & \mathbf{p}_t^M \\ \vdots & \ddots & \vdots \\ \mathbf{p}_{t+H}^1 & \cdots & \mathbf{p}_{t+H}^M \end{bmatrix}, \quad (16)$$

where $\mathbf{p}_{t+1}^i = \mathbf{p}_t^i + \mathbf{v}_t^i \Delta t$, $i = 1, \dots, M$, and Δt is the sample time. To transform this point flow $\mathbb{P}\mathbb{F}_t$ into the robot's local coordinate system $\widetilde{\mathbb{P}\mathbb{F}_t}$, we apply the rotation matrix $\mathbf{R}(s_t)$ and translation matrix $\mathbf{t}(s_t)$, calculated from the ego robot's state s_t as introduced in Eq. (5). Thus, the point flow $\widetilde{\mathbb{P}\mathbb{F}_t}$ in the robot's local coordinate system should be:

$$\widetilde{\mathbb{P}\mathbb{F}_t} = \begin{bmatrix} \tilde{\mathbf{p}}_t^1 & \cdots & \tilde{\mathbf{p}}_t^M \\ \vdots & \ddots & \vdots \\ \tilde{\mathbf{p}}_{t+H}^1 & \cdots & \tilde{\mathbf{p}}_{t+H}^M \end{bmatrix}, \quad (17)$$

where $\tilde{\mathbf{p}}_{h+1}^i = \mathbf{R}(s_h)^{-1}(\mathbf{p}_h^i - \mathbf{t}(s_h))$, for $h = t, \dots, t + H$. This transformed point flow $\widetilde{\mathbb{P}\mathbb{F}_t}$ is then fed into the deep unfolded neural encoder (DUNE), which leverages a neural encoder to map the point flow $\widetilde{\mathbb{P}\mathbb{F}_t}$ to generate the LDFs

$\mathcal{M} = \{\boldsymbol{\mu}_t^i \in \mathbb{R}^l\}$ and $\mathcal{L} = \{\boldsymbol{\lambda}_t^i \in \mathbb{R}^n\}$ with $\{\mathcal{M}, \mathcal{L}\} \in \mathcal{G}$. The encoder is denoted as deep unfolded neural encoder, since it can be interpreted as unfolding PIBCD into the DNN. Consequently, this network is both simple and fast, capable of handling thousands or more input points. This block is detailed in Section V-A.

2) Learnable model-based block: The model-based block seamlessly incorporates the LDFs into a motion planning optimization problem as a rigorously-derived regularizer, $C_r(\mathcal{S}, \bar{\mathcal{M}}, \bar{\mathcal{L}})$, imposed on the loss function C_0 , accounting for the reward of collision avoidance. With this regularizer, we can safely remove the numerous point-level collision avoidance constraints, which is in contrast to conventional approximation or regularization methods [21]–[23] that may lead to approximation error. The resultant problem is neural regularized, hence its associated solver is called neural regularized motion planner (NRMP). By leveraging functional differentiation, NRMP is also learnable, supporting auto-tuning of parameters in an end-to-end manner. This block is detailed in Section V-B.

3) End-to-End Algorithm: Our framework belongs to the generalized end-to-end approach because of the following reasons. 1) Our primal optimization problem is an end-to-end MPPC problem, which takes raw sensor data (i.e., points) as input and directly generates actions as output, aligning with typical end-to-end methods, such as those in [13], [39], where system components are jointly optimized to achieve the final objective. 2) The MPPC problem is solved by intertwined optimization of motion aware model predictive perception (i.e., DUNE) and perception regularized model predictive control (i.e. NRMP), which is derived from an equivalent transformation of the primal end-to-end MPPC problem. Intuitively, obstacle points are directly mapped to explainable LDFs to generate control commands, without involving any intermediate feature extraction step. 3) The system can be trained by end-to-end backpropagation to find the fine-tuned parameters in optimization block (detailed in Section VI-A3), aligning with typical end-to-end methods [13], [39]. This enables our approach to directly learn from rewards provided by the environments, thereby overcoming the issues of domain variations.

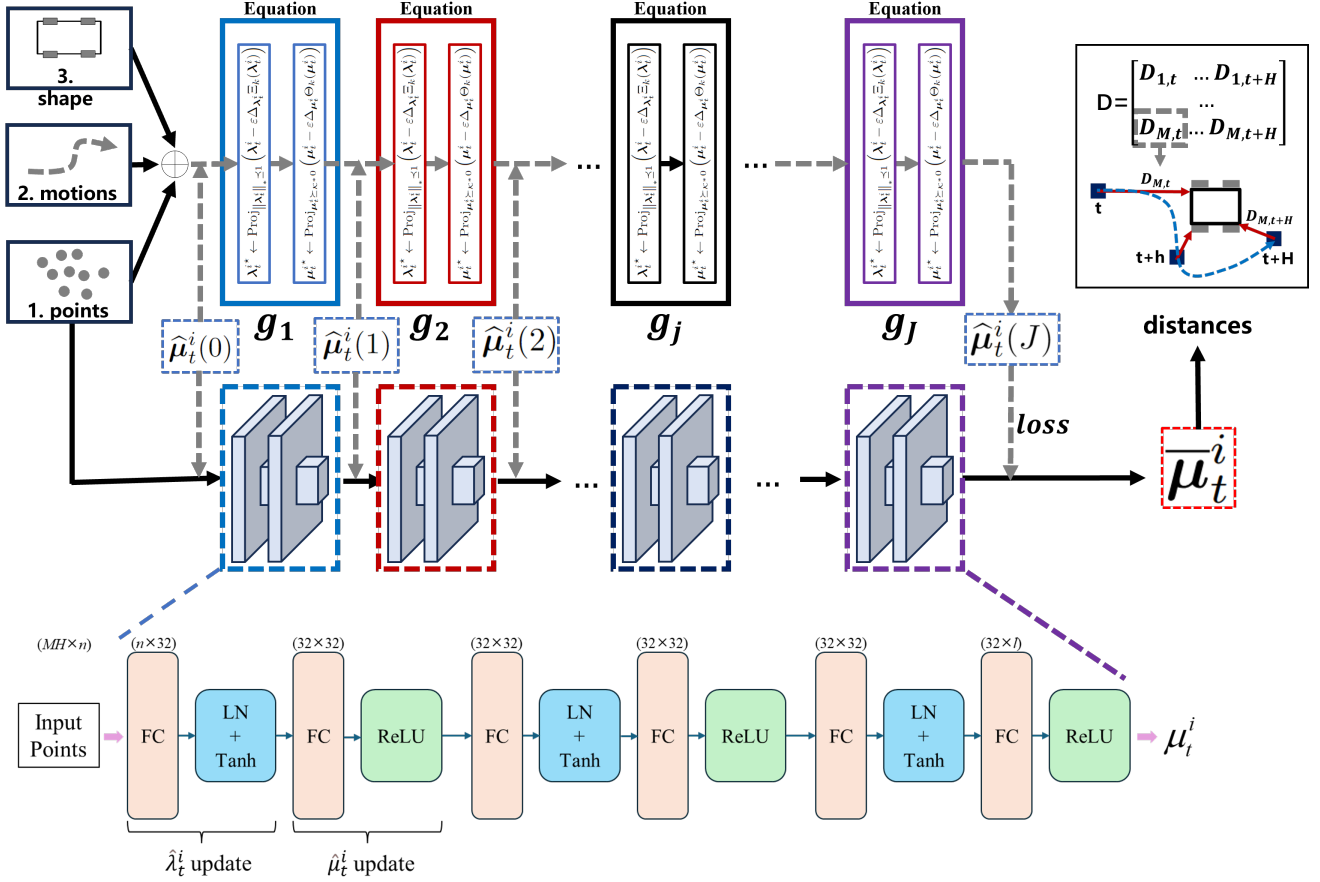


Fig. 5: Structure of DUNE, which unfolds the PIBCD algorithm. DUNE is explainable, simple, and fast to train, and can be deployed across various scenarios without retraining, provided the robot’s shape remains unchanged.

V. NEUPAN ENCODER AND PLANNER DESIGN

A. Deep Unfolded Neural Encoder

This subsection presents DUNE, which corresponds to solving Q_1 using, for example, $\{\bar{\mathcal{S}} = \mathcal{S}^{[k-1]}, \bar{\mathcal{U}} = \mathcal{U}^{[k-1]}\}$ at the k -th iteration. The nature of this subproblem is to convert each point to its corresponding LDF. The benefits of using such a transformation for the front-end are twofold: 1) LDFs can be directly incorporated into the subsequent NRMP network; 2) Mapping from points to LDFs can be realized by interpretable neural networks, as shown later. To explain how DUNE works, we will first derive the mathematical model of mapping from points to LDFs. Specifically, to guarantee collision avoidance at any time within the receding horizon of length H , it is necessary to compute the optimal $\{\mu_t^{i*}\}$ for any $t \in [t, t+H]$ and $i \in [0, M]$. The inference mapping from points to LDFs for all points $\{i\}$ and time slots $\{t\}$ is thus to solve $M \times H$ problems in parallel, each having a similar formula as Eq. (18). This leads to a total computational complexity of $\mathcal{O}(MHI^{3.5})$ by using CVXPY ECOS [40] and $\mathcal{O}(MHI)$ by using a penalty inexact block coordinate descent (PIBCD) algorithm, making it impossible for real-time applications, when M is in the range of thousands or more. To address this problem, we further unfold PIBCD into an explainable DNN, and obtain the architecture of DUNE, which can be viewed as a neural accelerated version of PIBCD.

1) *PIBCD for MAMPP Problem*: The MAMPP problem Q_1 can be simplified and written as the penalizing form of Eq. (12):

$$\begin{aligned} Q_1 : \min_{\mu_t^i, \lambda_t^i} & C_{\text{DUNE}}(\mu_t^i, \lambda_t^i), \\ \text{s.t.} & \mu_t^i \succeq_{\mathcal{K}^*} 0, \quad \|\lambda_t^i\|_* \leq 1, \end{aligned} \quad (18)$$

in which

$$\begin{aligned} C_{\text{DUNE}}(\mu_t^i, \lambda_t^i) = & -\mu_t^{i\top} (\mathbf{G}\tilde{\mathbf{p}}_t^i(\bar{\mathbf{s}}_t) - \mathbf{h}) \\ & + \underbrace{\rho \|\mu_t^{i\top} \mathbf{G} + \lambda_t^{i\top} \mathbf{R}_t(\bar{\mathbf{s}}_t)\|_2^2}_{\text{penalty term}}, \end{aligned} \quad (19)$$

where ρ is a sufficiently large penalty parameter, e.g., $\rho = 10^3$. Due to strong convexity, Eq. (18) can be optimally solved via inexact block coordinate descent optimization, which updates μ_t^i using gradient descent with λ_t^i fixed, and vice versa.

At the j -th iteration of PIBCD, given the solution $\hat{\mu}_t^i(j-1)$ at the $(j-1)$ -th iteration, the problem related to λ_t^i is

$$\min_{\lambda_t^i} \Xi_j(\lambda_t^i), \quad \text{s.t.} \quad \|\lambda_t^i\|_* \leq 1, \quad (20)$$

which is a quadratic minimization problem under norm ball constraints, with

$$\Xi_j(\lambda_t^i) = \|\hat{\mu}_t^i(j-1)^\top \mathbf{G} + \lambda_t^{i\top} \mathbf{R}_t(\bar{\mathbf{s}}_t)\|_2^2.$$

The associated one-step projected gradient descent update is

$$\lambda_t^{i*} \leftarrow \text{Proj}_{\|\lambda_t^i\|_* \leq 1} \left(\lambda_t^i - \varepsilon \Delta_{\lambda_t^i} \Xi_j(\lambda_t^i) \right), \quad (21)$$

where ε is the step-size. With the updated λ_t^{i*} , the problem related to μ_t^i is

$$\begin{aligned} \min_{\mu_t^i} \quad & \Theta_j(\mu_t^i) \\ \text{s.t.} \quad & \mu_t^i \succeq_{\mathcal{K}^*} 0, \end{aligned} \quad (22)$$

which is a quadratic minimization problem under box constraints, with

$$\Theta_j(\mu_t^i) = \rho \|\mu_t^{i* \top} \mathbf{G} + \lambda_t^{i* \top} \mathbf{R}_t(\bar{\mathbf{s}}_t)\|_2^2 - \mu_t^{i* \top} (\mathbf{G}\tilde{\mathbf{p}}_t^i(\bar{\mathbf{s}}_t) - \mathbf{h}).$$

The associated one-step projected gradient descent update is

$$\mu_t^{i*} \leftarrow \text{Proj}_{\mu_t^i \succeq_{\mathcal{K}^*} 0} \left(\mu_t^i - \varepsilon \Delta_{\mu_t^i} \Theta_j(\mu_t^i) \right). \quad (23)$$

This completes one iteration. By setting $\hat{\mu}_t^i(j) = \mu_t^{i*}$, we can proceed to solve the problem for the j -th iteration. According to [41], the sequence $\{\hat{\mu}_t^i(0), \hat{\mu}_t^i(1), \dots\}$ generated by the above iterative procedure is convergent, and converges to the optimal solution of Eq. (18).

To address the complexity issue while preserving interpretability, we propose a deep unfolding neural network to implement the point-LDF mapping. The detailed derivation is given below.

2) *Deep Unfolding Architecture*: The sequence $\{\hat{\mu}_t^i(0), \hat{\mu}_t^i(1), \dots\}$ generated by the PIBCD can be viewed as sequential mappings

$$\hat{\mu}_t^i(0) \xrightarrow{g_1} \hat{\mu}_t^i(1) \xrightarrow{g_2} \hat{\mu}_t^i(2) \dots \xrightarrow{g_J} \hat{\mu}_t^i(J) \quad (24)$$

These mappings $\{g_1, g_2, \dots\}$ are all gradient mappings. More specifically, g only consists of gradients of quadratic functions, which are matrix multiplication operations. Consequently, each g_i can be safely unfolded into neural network layers that also correspond to matrix multiplications. The required number of iterations J for PIBCD to converge determines the number of layers in the neural network. As such, deep unfolding takes a step towards interpretability by designing DNNs as learnt variations of iterative optimization algorithms.

Based on the above observations, the architecture of the proposed DUNE is shown in Fig. 5. The first layer is an $n \times 32$ fully connected layer that reads the positions of $M \times H$ points in a batch manner from the point flow. Following the first fully connected layer, Layer normalization (LN) and hyperbolic tangent function (Tanh) activation are implemented. This layer is obtained by unfolding Eq. (21), which is a one-step gradient descent update projected onto the l_2 norm ball. The second layer is an 32×32 fully connected (FC) layer followed by Rectified Linear Unit (ReLU) activation. This layer is obtained by unfolding Eq. (23), which is a one-step gradient descent update projected on the positive semidefinite cone (in the case of polygonal robots). By alternately repeating the first and second layers with 32 units alternatively ($J = 3$), the subsequent layers are constructed. Finally the output layer is a $32 \times l$ FC layer to output $\hat{\mu}_t^i$, and the entire DUNE network is equivalent to unfolding the PIBCD method for solving Q_1 . This is because PIBCD is an algorithm that

computes Eq. (21) and Eq. (23) alternatively, while DUNE is a network that computes unfolded layers of Eq. (21) and Eq. (23) alternatively.⁴

3) *Loss Function Design*: The neural network is trained using a labeled dataset derived from the PIBCD algorithm. Backpropagation is determined based on a loss function between the optimal solution, $\{\hat{\mu}_t^i\}$, and the neural network's solution, $\{\bar{\mu}_t^i\}$. A naive choice of the loss function is the mean square error (MSE) between these two values. However, since the learnt $\{\bar{\mu}_t^i\}$ will be used in the subsequent motion planning as a regularizer for tackling the collision avoidance constraints, we must guarantee high accuracy of $\{\bar{\mu}_t^i\}$ in different vector directions and incorporate these MSEs into the loss functions. Based on these considerations, we formulate the loss function as follows:

$$\begin{aligned} \mathcal{L}(\hat{\mu}_i, \bar{\mu}_i) = & \|\hat{\mu}_i - \bar{\mu}_i\|_2^2 + \|f_o(\hat{\mu}_i) - f_o(\bar{\mu}_i)\|_2^2 \\ & + \|f_a(\hat{\mu}_i) - f_a(\bar{\mu}_i)\|_2^2 + \|f_b(\hat{\mu}_i) - f_b(\bar{\mu}_i)\|_2^2, \end{aligned} \quad (25)$$

where, $f_o(\mu_i) = \mu_i^{\top} (\mathbf{G}\tilde{\mathbf{p}}_t^i - \mathbf{h})$ is the objective function of problem Eq. (12). Functions $f_a(\mu_i) = -\mu_i^{\top} \mathbf{G}\mathbf{R}_t^{\top}$ and $f_b(\mu_i) = \mu_i^{\top} \mathbf{G}\mathbf{R}_t^{\top} \tilde{\mathbf{p}}_t^i - \mu_i^{\top} \mathbf{h}$ are associated with the neural regularizer function C_r , which will be introduced in Section V-B.

4) *DUNE Training*: The hyperparameters for training the DUNE model are listed in Table II. For a robot with the given value $[\mathbf{G}, \mathbf{h}]$ (decided by the shape size), the training process starts with generating N_g point positions $\tilde{\mathbf{p}}$ randomly within a specific range $[\mathbf{r}_l, \mathbf{r}_h]$ in each axis. Subsequently, N_g convex optimization problems respecting to the variable μ are constructed by the known values of $[\mathbf{G}, \mathbf{h}, \tilde{\mathbf{p}}^i]$ and solved by the PIBCD algorithm or CVXPY ECOS, resulting in N_g optimal values μ^{i*} . As such, each point position $\tilde{\mathbf{p}}^i$ has a one-to-one corresponding optimal solution μ^i , resulting in a labeled dataset $\mathcal{T} = \{\tilde{\mathbf{p}}^i, \hat{\mu}_t^i\}$ for neural network training. The training process is conducted for e epochs with a batch size of B_n . The Adam optimizer is leveraged to update the network parameters using a learning rate of l_r and decay rate of d_r . In our experiment, the training process is conducted on a desktop computer with an AMD Ryzen 9 CPU and an NVIDIA GeForce GTX 4090 GPU. The training process takes approximately an hour to complete. The process is listed in algorithm 1.

Note that unlike typical deep learning models which require extensive data collection in real-world environments and may struggle with generalization due to the sim-to-real gap, our DUNE model is resilient to these challenges and can be trained rapidly because of its unique point representation and model-unfolded network structure. Furthermore, according to Eq. (12), the DUNE model is influenced solely by $[\mathbf{G}, \mathbf{h}]$, which are determined by the shape size. Consequently, for a specific robot, the DUNE model can be deployed across various real-world environments without the need for retraining.

⁴ $\hat{\lambda}_t^i$ can be derived from output $\hat{\mu}_t^i$ by the relationship in Eq. (12). $\hat{\lambda}_t^i = -\hat{\mu}_t^i \mathbf{G}^{\top} \mathbf{R}(\mathbf{s}_t)$.

TABLE II: Hyper-parameters used in DUNE training

Parameters	Value	Parameters	Value
N_g	100000	l_r	5e-5
$[\mathbf{r}_l, \mathbf{r}_h]$	[-25, 25]	d_r	0.5
B_n	256	e	5000

Algorithm 1: Deep Unfolded Neural Encoder (DUNE)

```

1 Input: Robot shape  $\{\mathbf{G}, \mathbf{h}\}$  and randomly generated
   point set  $\tilde{\mathbf{p}}_t^i(\mathbf{s}_t)$  within a specific range in the
   ego-robot coordinate system;
2 Initialize:  $\hat{\boldsymbol{\mu}}_t^i(0) \succeq_{\mathcal{K}^*} 0$ ;
3 for iteration  $j = 1, 2, \dots, J$  do
4   | Compute  $\boldsymbol{\lambda}_t^{i*}$  using Eq. (21);
5   | Compute  $\boldsymbol{\mu}_t^{i*}$  using Eq. (23);
6   | Set  $\hat{\boldsymbol{\mu}}_t^i(j) = \boldsymbol{\mu}_t^{i*}$  and  $j \leftarrow j + 1$ .
7   | if convergence then
8     | break
9   | end
10 end
11 Set training dataset  $\mathcal{T} = \{\tilde{\mathbf{p}}_t^i, \hat{\boldsymbol{\mu}}_t^i(J)\}$ ;
12 for epoch  $e = 1, 2, \dots, E$  do
13   | Calculate the loss function Eq. (25);
14   | Back propagation using  $\mathcal{T}$ ;
15   | if loss converges then
16     | break
17   | end
18 end
19 Output: DUNE model.

```

B. Neural Regularized Motion Planner

This subsection presents NRMP, which corresponds to solving the PRMPC problem Q_2 with fixed $\overline{\mathcal{M}} = \{\overline{\boldsymbol{\mu}}_t^i\}$ and $\overline{\mathcal{L}} = \{\overline{\boldsymbol{\lambda}}_t^i\}$ generated from the upstream DUNE. Owing to the efficient exact distance computation from DUNE, we can easily sort the importance of the obstacle points according to the distance. As such, we can reduce the computational complexity by only considering the M' closest points for the regularizer in each time step. This leads to the following problem

$$\begin{aligned}
Q_2 : \min_{\{\mathcal{S}, \mathcal{U}\} \in \mathcal{F}} & C_0(\mathcal{S}, \mathcal{U}) + \underbrace{C_r(\mathcal{S}, \overline{\mathcal{M}}, \overline{\mathcal{L}})}_{\text{neural regularizer}} \\
& + \underbrace{\frac{b_k}{2} \sum_{h=t}^{t+H} \|\mathbf{s}_h - \bar{\mathbf{s}}_h\|_2^2}_{\text{proximal term}}, \quad (26)
\end{aligned}$$

where $\bar{\mathbf{s}}$ is short for $\mathbf{s}^{[k-1]}$ obtained from the last iteration of NeuPAN, and b_k is the associated proximal coefficient at NeuPAN iteration k . This subproblem aims to generate collision-free robot actions efficiently by LDF-integrated regularizers.

1) *Neural Regularizer:* The regularization function based on Eq. (13) is

$$\begin{aligned}
C_r(\mathcal{S}, \overline{\mathcal{M}}, \overline{\mathcal{L}}) &= \frac{\rho_1}{2} \sum_{h=t}^{t+H} \sum_{i=0}^{M'} \left\| \min(I(\mathbf{s}_h, \overline{\boldsymbol{\mu}}_h^i, \overline{\boldsymbol{\lambda}}_h^i), 0) \right\|_2^2 \\
&+ \frac{\rho_2}{2} \sum_{h=t}^{t+H} \sum_{i=0}^{M'} \left\| E(\mathbf{s}_h, \overline{\boldsymbol{\mu}}_h^i, \overline{\boldsymbol{\lambda}}_h^i) \right\|_2^2,
\end{aligned}$$

In particular, C_r has the following properties:

- (i) C_r is a nonlinear but low-dimensional convex function of $\{\mathbf{s}_t\}$.
- (ii) C_r is a function of $\overline{\mathcal{M}} = \{\overline{\boldsymbol{\mu}}_t^i\}$ and $\overline{\mathcal{L}} = \{\overline{\boldsymbol{\lambda}}_t^i\}$ generated from the upstream neural encoder DUNE. That is why we call C_r “neural regularizer”.
- (iii) In practice, based on the relationship between $\boldsymbol{\lambda}_t^i$ and $\boldsymbol{\mu}_t^i$ guaranteed by DUNE, $\boldsymbol{\lambda}_t^i = -\boldsymbol{\mu}_t^i \mathbf{G}^\top \mathbf{R}(\mathbf{s}_t)$, C_r can be simplified by removing the penalty function E (set $\rho_2 = 0$)

Problem Q_2 is a low-dimensional convex optimization program due to: convexity of norm function C_0 in Eq. (10), linearity of \mathcal{F} , and property (i) of C_r . Consequently, Q_2 can be optimally solved via the off-the-shelf software for solving convex problems, e.g., cvxpy ECOS. In practice, a static safety distance d_{\min} may not be suitable for time-varying environments. As a consequence, d_{\min} in Q_2 needs to be dynamically adjusted. To achieve this goal, we propose to use a variable distance d_t to replace d_{\min} in penalty function I , where d_t is within the range $[d_{\min}, d_{\max}]$. To encourage d_t to approach d_{\min} in highly-confined spaces and to approach d_{\max} in highly-dynamic environments, we propose a sparsity-induced distance regularizer $C_1(\mathbf{d}) = -\eta \sum_{h=t}^{t+H} \|\mathbf{d}_h\|_1$, where η is a weighting factor. As such, $C_1(\mathbf{d})$ introduces adaptation to collision [20]. Consequently, this would involve manually tuning parameters $\mathcal{P} = \{\mathbf{q}, \mathbf{p}, d_{\min}, d_{\max}, \eta\}$ in C_0 , C_r , and C_1 . The next subsection will derive a learnable optimization method to fine tune \mathcal{P} automatically.

2) *Learnable Optimization Network:* The weight parameters in optimization problems are usually manually tuned, which is time-consuming and may not be optimal for challenging scenarios. In order to enable automatic calibration of parameters in Q_2 under new environments, we present a *learnable optimization network* (LON) approach for solving Q_2 , which can learn from failures to find the proper parameters. The crux of LON is that it leverages differentiable convex optimization layers (cvxpylayers) [42]. As such, in contrast to traditional optimization solvers, LON offers the ability to differentiate through disciplined convex programs. Within these programs, parameters can be mapped directly to solutions, facilitating backpropagation calculations. Moreover, with cvxpylayers, the NRMP can be seamlessly integrated with the DUNE, as both of them support back propagation, thereby enabling end-to-end training of the entire NeuPAN system.

However, solving Q_2 using LON is nontrivial, since cvxpylayers require the optimization problem to satisfy disciplined parametrized program (DPP) form. To this end, this paper proposes the following problem reconfiguration that recasts Q_2 into a DPP-friendly problem. In particular, to satisfy the

DPP formats in [42], we reconfigure the non-DPP function C_0 by introducing a set of DPP parameters $\{\gamma_t^a, \gamma_t^b\}$, which gives

$$C_0^{\text{DPP}}(\mathcal{S}, \mathcal{U}) = \sum_{h=t}^{t+H} \left(\|\mathbf{q} \circ \mathbf{s}_h - \gamma_h^a\|_2^2 + \|\mathbf{p} \circ \mathbf{u}_h - \gamma_h^b\|_2^2 \right), \quad (27)$$

where $\gamma_h^a \leftarrow \mathbf{q} \circ \mathbf{s}_h^\diamond$ and $\gamma_h^b \leftarrow \mathbf{p} \circ \mathbf{u}_h^\diamond$ are introduced as DPP parameters for back propagation⁵. On the other hand, we reformulate C_r in \mathcal{Q}_2 as

$$C_r^{\text{DPP}}(\mathcal{S}, \mathcal{U}, \mathcal{L}) = \frac{\rho_1}{2} \sum_{h=0}^{H-1} \sum_{i=0}^M \|\min(I^{\text{DPP}}(\mathbf{s}_h, \boldsymbol{\mu}_h^i, \boldsymbol{\lambda}_h^i), 0)\|_2^2 + \frac{\rho_2}{2} \sum_{h=0}^{H-1} \sum_{i=0}^M \|E^{\text{DPP}}(\mathbf{s}_h, \boldsymbol{\mu}_h^i, \boldsymbol{\lambda}_h^i)\|_2^2, \quad (28)$$

where the DPP-reformulated I and E are

$$I^{\text{DPP}} = {}^c \gamma_t^i \mathbf{t}_t(\mathbf{s}_t) - {}^a \xi_t^i - d_t, \quad (29)$$

$$E^{\text{DPP}} = {}^d \gamma_t^i + {}^c \gamma_t^i \mathbf{R}_t(\mathbf{s}_t), \quad (30)$$

with vector $\gamma_t^i \leftarrow \boldsymbol{\lambda}_t^{\top} \mathbf{p}_t + \boldsymbol{\mu}_t^{\top} \mathbf{h}$, and scalar $\xi_t^i \leftarrow \boldsymbol{\lambda}_t^{\top} \mathbf{p}_t + \boldsymbol{\mu}_t^{\top} \mathbf{h}$. Thus, the DPP parameters are $\mathcal{P} = \{\mathbf{q}, \mathbf{p}, d_{\min}, d_{\max}, \eta, \bar{\mathbf{s}}_h, \gamma_t^a, \gamma_t^b, \gamma_t^c, \gamma_t^d, \xi_t^a, \xi_t^b\}$. Considering the impact on the generated behavior, we selected $\mathcal{P}' = \{\mathbf{q}, \mathbf{p}, d_{\min}, d_{\max}, \eta\}$ as the learnable parameters in LON.

With the above reconfiguration, problem \mathcal{Q}_2 becomes

$$\mathcal{Q}_2^{\text{DPP}} : \min_{\{\mathcal{S}, \mathcal{U}\} \in \mathcal{F}} C_0^{\text{DPP}}(\mathcal{S}, \mathcal{U}) + C_r^{\text{DPP}}(\mathcal{S}, \bar{\mathcal{M}}, \bar{\mathcal{L}}) + C_1(\mathbf{d}) + \frac{b_k}{2} \sum_{h=0}^{H-1} \|\mathbf{s}_h - \bar{\mathbf{s}}_h\|_2^2. \quad (31)$$

It can be proved that both C_0^{DPP} , C_r^{DPP} , and $C_1(\mathbf{d})$ satisfy the DPP regulation. Adding to the fact that other functions in set \mathcal{F} are DPP-friendly, problem $\mathcal{Q}_2^{\text{DPP}}$ is DPP compatible, whose parameters can be optimized using the back propagation. Specifically, a parameter, say $x \in \mathcal{P}'$, can be revised utilizing the gradient descent method, facilitated by a loss function $L(\mathcal{P})$, as follows:

$$x^{(k+1)} = x^{(k)} - \alpha \frac{\partial L}{\partial x} \quad (32)$$

where, α is the learning rate. The gradient is clipped within a range $[g_{\min}, g_{\max}]$, with the maximum value of 1.0 to avoid the gradient explosion.

3) *Loss Function*: The loss function $L(\mathcal{P})$ is designed based on the cost function C_0 , C_r , and C_1 presented in $\mathcal{Q}_2^{\text{DPP}}$ and can be selected depending on a specific task. Particularly, the final loss function could be the combination of several atom loss functions: $L(\mathcal{P}') = \sum_{i=0} a_i L_i(\mathcal{P}')$, where a_i is the weight of the i -th loss function. The key idea is to allow the

Algorithm 2: DPP-friendly NRMP

- 1 **Input**: LDFs $\{\bar{\mathcal{M}}, \bar{\mathcal{L}}\}$ from DUNE;
 - 2 Robot Geometry information $[\mathbf{G}, \mathbf{h}]$;
 - 3 Construct parametrized convex optimization problem;
 - 4 Initialize the learnable parameters
 $\mathcal{P}' = \{\mathbf{q}, \mathbf{p}, d_{\min}, d_{\max}, \eta\}$.
 - 5 Solve the problem Eq. (31) via DPP solver;
 - 6 **if** failures returns True **then**
 - 7 | Update NRMP via back propagation by loss
| function $L(\mathcal{P}')$
 - 8 **end**
 - 9 **Output**: State and action sequence $[\mathcal{S}, \mathcal{U}]$.
-

LON to learn from failures to update the learnable parameters. Here, we provide three examples of the atom loss functions:

$$\begin{cases} L_1(\mathcal{P}') = \|\mathbf{s} - \mathbf{s}^\diamond\|_2^2, \\ L_2(\mathcal{P}') = \|\mathbf{u} - \mathbf{u}^\diamond\|_2^2 \\ L_3(\mathcal{P}') = -\eta \sum_{h=t}^{t+H} \|\mathbf{d}_h\|_1, \end{cases}$$

- If the robot strays from the destination, the $L_1(\mathcal{P}')$ function can be used to yield a larger \mathbf{q} , and encourage the robot to return to the naive path.
- If the robot gets stuck in a congested environment, the $L_2(\mathcal{P}')$ and $L_3(\mathcal{P}')$ can be combined to yield a larger \mathbf{p} but a smaller d_{\max} which creates an incentive for robot motion.
- If the robot collides with obstacles, the $L_1(\mathcal{P}')$ and $L_3(\mathcal{P}')$ can be combined to yield a smaller \mathbf{q} , allowing the robot to temporarily leave the naive path, and a larger d_{\max} producing more conservative movements.

The entire procedure of NRMP is summarized in Algorithm 2.

C. Convergence and Complexity Analysis

The entire NeuPAN procedure is summarized in Algorithm 3, which can be viewed as iterations between learning-based (i.e., DUNE) and model-based (i.e., NRMP) algorithms. Specifically, given $\{\mathcal{S}^{[k]}, \mathcal{U}^{[k]}\}$ of state-action space at the k -th iteration, NeuPAN generates the next-round solution $\{\mathcal{S}^{[k+1]}, \mathcal{U}^{[k+1]}\}$ as follows:

$$\{\mathcal{S}^{[k]}, \mathcal{U}^{[k]}\} \xrightarrow{\text{DUNE}} \{\mathcal{M}^{[k+1]}, \mathcal{L}^{[k+1]}\} \xrightarrow{\text{NRMP}} \{\mathcal{S}^{[k+1]}, \mathcal{U}^{[k+1]}\}.$$

Consequently, starting from an initial guess $\{\mathcal{S}^{[0]}, \mathcal{U}^{[0]}\}$, the sequence generated by NeuPAN is

$$\begin{aligned} \{\mathcal{S}^{[0]}, \mathcal{U}^{[0]}\} &\xrightarrow{\text{DUNE}} \{\mathcal{M}^{[1]}, \mathcal{L}^{[1]}\} \xrightarrow{\text{NRMP}} \{\mathcal{S}^{[1]}, \mathcal{U}^{[1]}\} \\ &\xrightarrow{\text{DUNE}} \{\mathcal{M}^{[2]}, \mathcal{L}^{[2]}\} \xrightarrow{\text{NRMP}} \{\mathcal{S}^{[2]}, \mathcal{U}^{[2]}\} \\ &\xrightarrow{\text{DUNE}} \{\mathcal{M}^{[3]}, \mathcal{L}^{[3]}\} \dots \end{aligned} \quad (33)$$

Such model-based deep learning framework can be trained via end-to-end back propagation. It can naturally exploit additional training data by adding neurons to DUNE and prior knowledge by adding constraints to NRMP.

⁵The symbol \leftarrow represents parameter substitution

Algorithm 3: NeuPAN

```

1 Input: Robot geometry information  $[G, h]$ ;
2   Current robot states  $\bar{s}_t$ ;
3   Current point cloud  $\mathbb{P}_t$ ;
4   Well-trained neural encoder DUNE;
5   Parametrized optimization network NRMP;
6   Naive path  $\{s_{\text{start}}, s_0^\diamond, s_1^\diamond, \dots, s_{\text{goal}}\}$ 
7 Initialize  $\mathcal{S}^{[0]}$  and  $\mathcal{U}^{[0]}$ .
8 for iteration  $k = 0, 1, 2, \dots$  do
9   Generate point flow  $\widehat{\mathbb{P}\mathbb{F}}$  from the current scan  $\mathbb{P}_t$ 
   and robot motion  $\mathcal{S}^{[k]}$ ;
10  Generate the latent distance features  $\{\overline{\mathcal{M}}, \overline{\mathcal{L}}\}$  via
   DUNE;
11  Generate the state-action variables  $\{\overline{\mathcal{S}}, \overline{\mathcal{U}}\}$  via
   NRMP;
12  Update  $\{\mathcal{M}^{[k+1]} = \overline{\mathcal{M}}, \mathcal{L}^{[k+1]} = \overline{\mathcal{L}}\}$ ;
13  Update  $\{\mathcal{S}^{[k+1]} = \overline{\mathcal{S}}, \mathcal{U}^{[k+1]} = \overline{\mathcal{U}}\}$ ;
14  if stopping criteria are satisfied, then
15    | break;
16  end
17  Update  $k \leftarrow k + 1$ ;
18 end
19 Output: Control vector and associated trajectory
    $\{\mathcal{U}, \mathcal{S}\}$ 

```

To see why NeuPAN works, the following theorem is established.

Theorem 1. *The sequence $[\{\mathcal{S}^{[0]}, \mathcal{U}^{[0]}\}, \{\mathcal{S}^{[1]}, \mathcal{U}^{[1]}\}, \dots]$ satisfies the following conditions:*

(i) *Monotonicity:* $C_{e2e}^{[0]} \geq C_{e2e}^{[1]} \geq C_{e2e}^{[2]} \geq \dots$, where $C_{e2e}^{[k]} = C_{e2e}(\mathcal{S}^{[k]}, \mathcal{U}^{[k]}, \mathcal{M}^{[k]}, \mathcal{L}^{[k]})$.

(ii) *Convergence:* $\|C_{e2e}^{[k+1]} - C_{e2e}^{[k]}\|_2 \rightarrow 0$ as $k \rightarrow \infty$.

(iii) *Convergence to a critical point of Q.*

Proof. See Appendix C (Supplementary Material). \square

Part (i) of **Theorem 1** states that adding the tightly-coupled feedback from the NRMP (i.e., motion) to the DUNE (i.e., perception) is guaranteed to improve the performance of the NeuPAN system (under the criterion of solving P). Part (ii) of **Theorem 1** means that we can safely iterate the loop, since the outputs converge and do not explode. Part (iii) of **Theorem 1** implies that the states and actions generated by NeuPAN must be at least a local optimal solution to Q, which is an equivalent problem to P. All the above insights indicate that the proposed algorithm has end-to-end mathematical guarantee, which is in contrast to all existing approaches.

Based on **Theorem 1**, we can terminate NeuPAN until convergence. In practice, to save the computation time and enable real-time end-to-end robot navigation, we terminate the NeuPAN iteration when the number of iterations reach the limit, e.g., $K = 3$.

Finally, we present the complexity analysis of NeuPAN. Depending on the procedure listed in Algorithm 3, in each iteration, the scan flow is first generated from the scan data with a complexity of $\mathcal{O}(MH)$. Subsequently, DUNE

consists of multiple neural layers at a computational cost of $\mathcal{O}(MHN_n)$, where N_n is the number of neurons in the DUNE neural network. Next is the NRMP, which solves a DPP based optimization problem with a complexity of $\mathcal{O}(H(n+2))^{3.5}$. In summary, with the number of iterations required to converge being K , the total complexity of NeuPAN is $\mathcal{O}(K(MH(N_n+1) + (H(n+2))^{3.5}))$. It can be seen that the complexity is linear with M which corroborates the facts that NeuPAN can tackle thousands of points in real-time.

VI. EXPERIMENTS

In this section, we present numerical results in an open source lightweight robot simulator, *Ir-sim*⁶, to analyze the effectiveness and efficiency of NeuPAN. To further demonstrate the effectiveness and robustness of NeuPAN under practical settings, we also evaluate the performance of NeuPAN on different robot platforms in high-fidelity simulation environments and real-world test tracks.

The adopted robot platforms include ground mobile robot, wheel-legged robot, and passenger autonomous vehicle, as depicted in Fig. 6.

- The ground mobile robot shown in Fig. 6(a) is a customized, multi-modal, small-size robot platform, whose motion kinematics can be switched between the differential and Ackermann modes.
- The wheel-legged robot shown in Fig. 6(b) is a mid-size platform that integrates the functionalities of both wheeled and legged robots, thus enjoying the joint benefits of high-mobility and terrain-adaptability in complex scenarios. Compared to the ground robot in Fig. 6(a), wheel-legged robots involve higher motion uncertainties (e.g., body oscillation), and thus requires more precise control to ensure stability.
- The passenger autonomous vehicle shown in Fig. 6(c) is a $4.675 \text{ m} \times 1.77 \text{ m} \times 1.5 \text{ m}$ large-size vehicle platform for urban driving.

All these platforms are equipped with lidar systems (2D or 3D), enabling them to obtain the point representation of the environment. Localization of these robots in unknown environments is realized by Fast-lio2 [43] or Lego-Loam [44], [45]. All the experiments are conducted without any prior map, relying solely on goal positions, desired speed, and onboard lidar for autonomous navigation. Note that in real-world experiments, the moving obstacles (e.g. humans) have low speed (less than 1 m/s), and we treat these obstacle points from laser scans as fixed during each MPPC horizon.⁷

We adopt the following performance metrics for evaluations.

- **Success rate:** Success is defined as the robot completing the navigation task without any collision. This includes two conditions, i.e., route completion and collision avoidance. Route completion is considered a failure if the

⁶Online. Available: https://github.com/hanruihua/ir_sim.

⁷In such a case, the movements of obstacles within a short MPPC horizon (i.e., tens of milliseconds) is negligible, and treating obstacles as fixed objects does not impact the system performance. Furthermore, our high control frequency enables the robot to perform agile behaviors by reacting to changes in the positions of low-speed obstacles.

TABLE III: Performance comparison of NeuPAN and RDA in the Ir-sim simulation

Kinematics	Scenarios	Success Rate		Average Navigation Time		Average Speed	
		Neupan	RDA	Neupan	RDA	Neupan	RDA
Ackermann	Convex Obstacles	86	90	136.99	145.87	3.80	3.74
	Nonconvex Obstacles	73	59	134.93	146.20	3.82	3.73
	Dynamic Obstacles	90	88	130.49	160.42	3.97	3.56
Differential	Convex Obstacles	97	97	135.18	146.75	3.97	3.76
	Nonconvex Obstacles	82	71	133.11	151.34	3.97	3.71
	Dynamic Obstacles	92	88	130.51	153.95	3.97	3.68

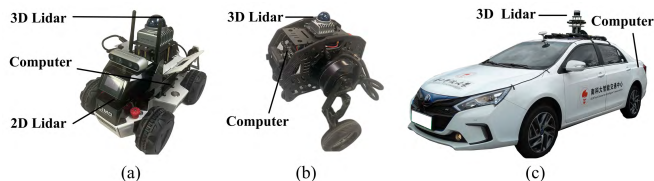


Fig. 6: Three types of robot platforms used in our experiments: (a) ground mobile robot; (b) wheel-legged robot; (c) autonomous driving vehicle.

navigation time exceeds a predefined threshold (indicating that the robot gets stuck). Meanwhile, any collision between the robot and obstacles is also considered a failure. A similar definition of success is presented in [6]. The success rate is the ratio of successful cases out of the total number of test trials.

- **Navigation time:** Navigation time refers to the amount of time for the robot to successfully complete the navigation task. It is measured by counting the time steps in the simulator or recording the timestamps in real-world experiments.
- **Average speed:** Average speed is calculated over the entire navigation process, as recorded by the simulator or the odometry in real-world experiments.

Higher success rate indicates better collision avoidance ability and effectiveness. Shorter navigation time and higher average speed indicate higher mobility and efficiency. To quantify the level of navigation difficulty in cluttered environments, we define a metric termed the **Degree of Narrowness (DoN)**, as follows:

$$\text{DoN} = \frac{\text{robot width}}{\text{minimum passable space width}} \quad (34)$$

Higher DoN (closer to 1) means a narrower space and a higher difficulty for robot pass through; and vice versa.

A. Experiment 1: Verification of NeuPAN in Ir-sim

1) *Comparison with RDA:* We test and compare the performance of NeuPAN and RDA [20] using differential and Ackermann robots in three different scenarios composed of 11 randomly generated convex, nonconvex, and dynamic obstacles (speed: 1 m/s). To ensure fair comparisons between NeuPAN and RDA, the robots equipped with 2D lidar are given the same start (i.e., [-1, 25]) and goal (i.e., [50, 25]) positions, with a desired speed of 4 m/s, as shown in Fig. 7. Quantitative

comparison results over 100 trials are listed in Table III. We evaluate the success rate, average navigation time, and average speed for both NeuPAN and RDA. The results demonstrate that when handling the convex obstacles, the success rates of RDA and NeuPAN are close to each other under both differential and Ackermann kinematics. However, when handling nonconvex obstacles, RDA achieves the success rates of 59% and 71%, while NeuPAN achieves the success rates of 73% and 82%, under Ackermann and differential kinematics, respectively. This indicates that NeuPAN outperforms RDA by over 19% in terms of the success rate for nonconvex obstacles. This result demonstrates the importance of directly mapping raw points to actions via NeuPAN. This also quantitatively illustrates how much navigation performances could be improved by representing obstacles as dense points. In addition, NeuPAN achieves higher moving speed (6.0% improvement) and less navigation time (11.27% reduction) in all the simulated scenarios as shown in Table III, which verifies the high efficiency of NeuPAN. More demonstrations in Ir-sim can be found in Appendix D (Supplementary Material).

2) *Impact of Obstacle Velocity:* To show the effectiveness of our approach in handling moving obstacles with known point velocities, we compare the performance of NeuPAN and NeuPAN-vel (incorporating point velocities) in the dynamic scenario shown in Fig. 7(c). We consider four different scenarios, with the velocities of obstacles ranging from 1 m/s to 4 m/s, and evaluate the performance metrics of success rate, average navigation time, and average speed. All the results in Table. IV are obtained by averaging 100 trials. It can be seen that the performance of NeuPAN and NeuPAN-vel is comparable in lower-speed scenarios (e.g., obstacles with velocities 1 m/s and 2 m/s). However, in the high-speed scenarios (e.g., obstacles with velocities 3 m/s and 4 m/s), NeuPAN-vel achieves higher success rates (with 10.96% and 35.42% improvements in the 3 m/s and 4 m/s cases, respectively) and shorter navigation time (with 1.09% and 3.47% reductions in the 3 m/s and 4 m/s cases, respectively), which demonstrates the effectiveness of incorporating point velocities into NeuPAN for handling moving obstacles.

3) *Verification of Fine-Tuning:* The proposed NeuPAN is able to learn from rewards provided by the environments, thereby handling domain variations (e.g., sensor noises) through auto-tuning. To see this, we consider a corridor scenario with DoN=0.67. Given start and goal positions [-5, 20] and [75, 20], respectively, the associated result is shown in Fig. 8. Initially, we configure NeuPAN with improper parameters and the robot experiences a collision at the episode 0

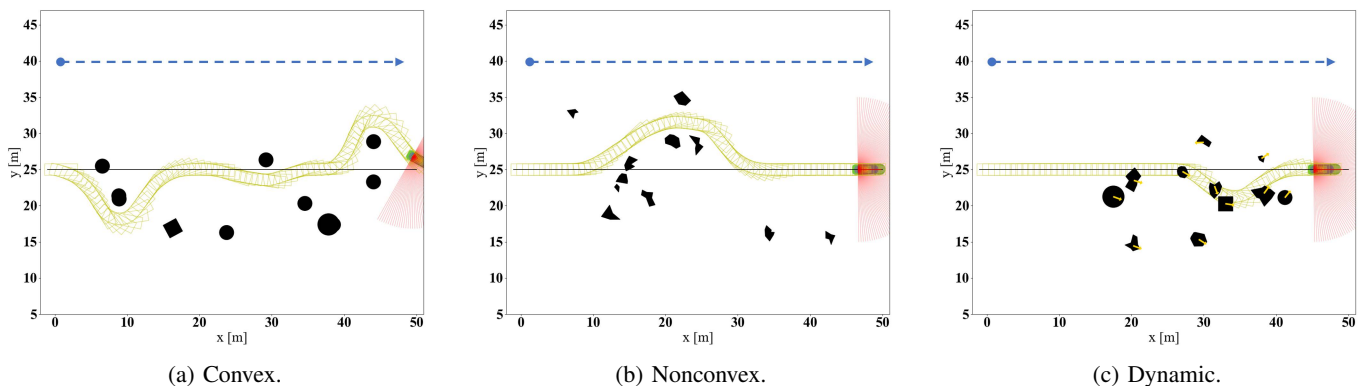


Fig. 7: Scenarios with randomly generated obstacles used to evaluate NeuPAN and RDA.

TABLE IV: Performance comparison of NeuPAN and NeuPAN-vel in the Ir-sim simulation.

Dynamic Obstacle Speed (m/s)	Success Rate		Average Navigation Time		Average Speed	
	Neupan	NeuPAN-vel	Neupan	NeuPAN-vel	Neupan	NeuPAN-vel
1	0.92	0.93	129.02	128.83	3.97	3.97
2	0.90	0.89	131.10	131.55	3.97	3.96
3	0.73	0.81	139.78	138.26	3.96	3.96
4	0.48	0.65	147.98	142.85	3.96	3.99

(i.e., the first subfigure of Fig. 8(a)). By back-propagation of failure using the loss function $L_3(\mathcal{P}')$, the robot is able to make progress after 27 and 38 training episodes (i.e., the second and third subfigures of Fig. 8(a)). After 54 episodes of training, the robot successfully navigates through the scenario with proper parameters (the last subfigure of Fig. 8(a)).

Subsequently, we test the well-trained NeuPAN in the same corridor scenario, but the robot lidar now involves sensor noises (i.e., Gaussian noise with standard deviation of 0.2 added to the ranging measurements). While the well-trained NeuPAN has the ability to tackle the noise-free case and pass the corridor, it struggles under the sensor noises and collides with obstacles, as shown in the left hand side of Fig. 8(b). However, if we continue training NeuPAN for another 12 episodes, the robot again navigates through the corridor. Even if the sensor noise is too large, causing the inner corridor becomes impassable, NeuPAN can still find an alternative outer path (right hand side of Fig. 8(b)). This demonstrates the adaptability of NeuPAN in handling domain variations.

The average training loss over the number of episodes is shown in Fig. 8(c). It can be seen that the loss decreases rapidly and converges to the minimal value under both perfect and noisy cases, which corroborates Fig. 8(a) and Fig. 8(b), and shows that the training speed is fast. This is due to the model-based learning nature of NeuPAN, which tunes only a small number of learnable parameters through back propagation as mentioned in Section V-B.

B. Experiment 2: Validation of DUNE on Open Datasets

In this subsection, real-world experiments are presented to verify the efficacy of our proposed DUNE block of NeuPAN as well as its advantage over existing methods adopting inexact distances (Supplementary Material Appendix E). We consider two open-source datasets: 1) KITTI [46], which is

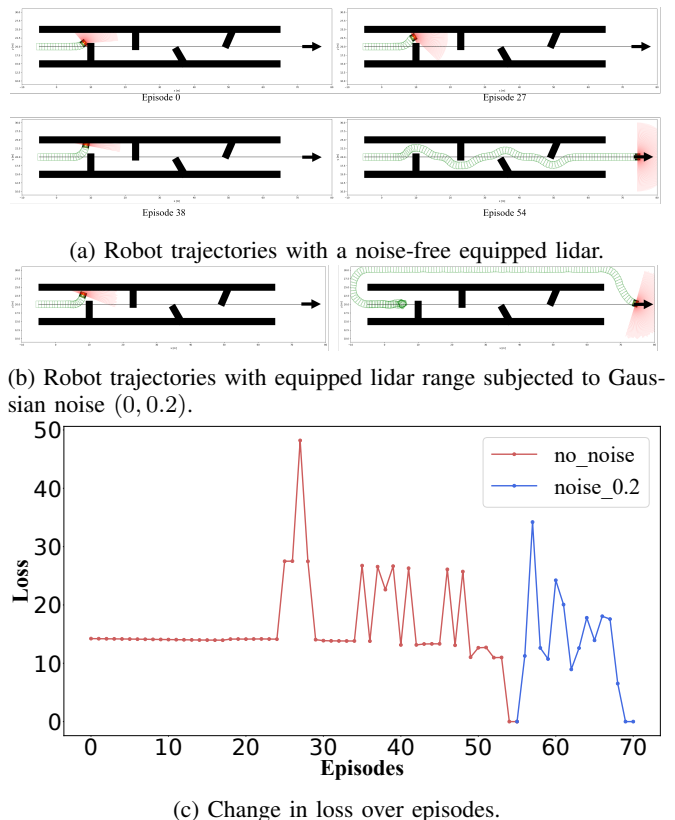


Fig. 8: Robot trajectories and training loss change over episodes.

a popular real-world urban driving dataset (see Fig. 9(a)); 2) SUSCAPE ⁸, which is a large-scale multi-modal dataset with

⁸Online. Available: <https://suscape.net/home>.

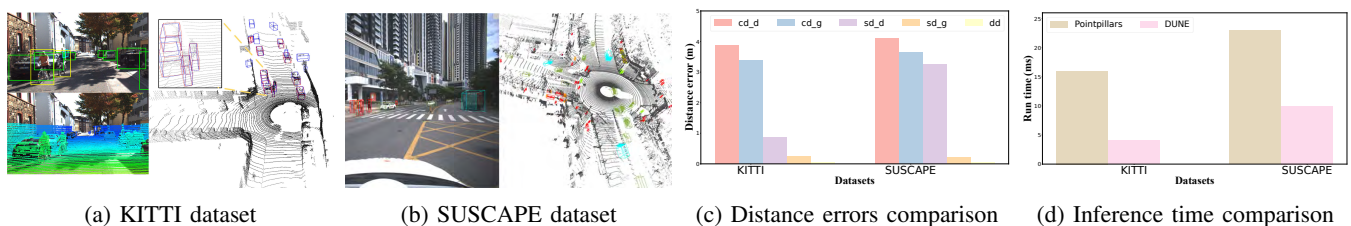


Fig. 9: Comparison of distance errors on KITTI and SUSCAPE datasets. (a) Object detection results by Pointpillars on KITTI. Blue and red boxes denote the detected result and the ground truth, respectively. (b) Perfect object detection results on SUSCAPE, where all boxes are labeled by human experts. (c) Average distance errors of cd, sd, and dd on KITTI and SUSCAPE. (d) Inference time comparison between DUNE and Pointpillars.

more than 1000 scenarios. This SUSCAPE dataset is collected and processed based on the autonomous vehicle platform in Fig. 6(c). We calculate the minimum distance between the ego-vehicle and all surrounding objects based on three different rules: center point distance (cd), full shape set distance (sd), and our DUNE distance (dd). The computations of cd and sd based on the boxes of the object detectors are denoted by cd_d and sd_d. Here we choose a celebrated point based detector Pointpillars [47], whose accuracy achieves 74.31% (moderate) for the car detection task. The distance error is defined by the difference between the calculated distance and the ground truth distance (computed based on the raw point cloud provided by the dataset). It can be seen from Fig. 9(a) and 9(c) that the distance error of DUNE block of NeuPAN is significantly smaller than the errors of the other approaches, which concisely quantify the benefit brought by direct point robot navigation. As such, we can effectively overcome the detection inaccuracies inherent in conventional object detection algorithms.

Qualitative results in the SUSCAPE dataset are shown in Fig. 9(b) and the associated quantitative results are shown in Fig. 9(c). The results show that our DUNE distance still has the smallest error. In addition, the cd_d and sd_d errors increase compared with the result in KITTI. This is due to the lack of the generalizability of the learning based object detector. In contrast, our DUNE block of NeuPAN can be directly applied across different datasets. Finally, one may wonder whether we can reduce this distance error by replacing Pointpillars with other highly accurate object detectors. To this end, we conduct another experiment of considering a perfect object detector with 100% accuracy, i.e., we directly use the ground truth bounding boxes labeled by human experts as its outputs. The computations based on this detector can be denoted by cd_g and sd_g. It can be seen from Fig. 9(c) that the errors of cd_g, sd_g are smaller than that of cd_d and sd_d due to the improvement in object detection. However, these errors are still much larger than the dd error. This is because there exist a gap between the shapes of a box and a nonconvex object.

The inference latencies of DUNE block of NeuPAN and Pointpillars on two datasets (tested using the same computer platform) are shown in Fig. 9(d). It can be seen that the inference time of DUNE achieves 4 ms in KITTI dataset and 10 ms in SUSCAPE dataset, respectively, which is much faster than the 16 ms and 23 ms inference time of Pointpillars. This

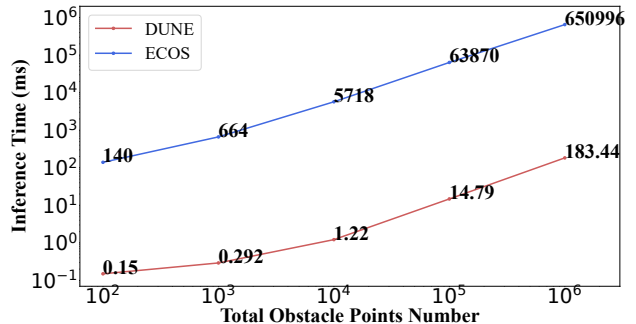


Fig. 10: Inference time comparison of DUNE and the optimization solver ECOS with varying number of input points.

is because DUNE is a fully explainable lightweight neural network with only six fully connected layers, which is much more efficient than Pointpillars network with deep convolution layers.

To analyze the scalability of DUNE block of NeuPAN, its computation time over the number of points is shown in Fig. 10. For comparison, we also implement a benchmark scheme ECOS [40], which is an off-the-shelf optimization solver for solving problem Eq. (12). All the tests are performed on a computer equipped with an AMD Ryzen 9 CPU. It can be seen that the proposed DUNE is able to handle 1 million points within 0.2 second. In contrast, the baseline approach ECOS requires more than 650 seconds for handling 1 million points, which is significantly higher than that of DUNE. This demonstrates that DUNE reduces the computation time by over 1000x when the number of input points is in the range of thousands or more. Such significant acceleration is due to the model-based learning nature of DUNE, which corroborates the theory and methodology in Section V-A.

C. Experiment 3: Ground Mobile Robot Navigation

1) *Dynamic Environment*: We adopt Gazebo [48], a widely recognized open-source 3D robotics simulator, to demonstrate the dynamic collision avoidance capability of our approach by using onboard 2D lidar. The experimental setup is illustrated in Fig. 11(a)- 11(b), where the robot, operating in differential steering mode, must patrol between two given checkpoints as fast as possible while preventing itself from being surrounded and collided by massive adversarial moving obstacles. The obstacles with cylinder and nonconvex shapes are randomly

TABLE V: Performance comparison of NeuPAN, RDA, and AEMCARL in Gazebo

Scenarios		Success Rate			Navigation Time			Average Speed		
		NeuPAN	RDA	AEMCARL	NeuPAN	RDA	AEMCARL	NeuPAN	RDA	AEMCARL
Cylinder Obstacles	10	0.93	0.89	0.89	35.61	38.51	53.45	0.285	0.280	0.259
	15	0.90	0.88	0.82	36.71	42.19	57.71	0.279	0.263	0.257
	20	0.88	0.82	0.73	38.17	46.03	61.21	0.264	0.246	0.221
Nonconvex Obstacles	10	0.90	0.70	-	37.91	45.25	-	0.273	0.266	-
	15	0.88	0.62	-	39.87	48.36	-	0.261	0.259	-
	20	0.85	0.59	-	42.47	50.09	-	0.255	0.228	-

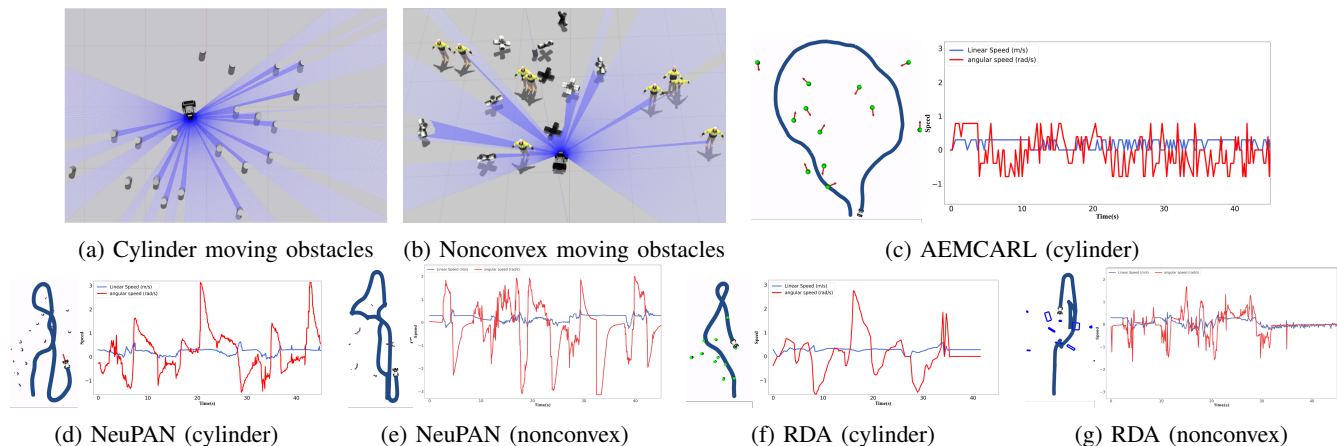


Fig. 11: Trajectory and speed profile comparisons of NeuPAN, RDA, and AEMCARL in Gazebo dynamic environment with cylinder and nonconvex moving obstacles.

placed within a region of interest and exhibit reciprocal collision avoidance behavior with speed adjustments (max speed: 0.1 m/s). We compare our method with the reinforcement learning based method AEMCARL [24] and optimization based method RDA [20]. All these methods adopt a desired speed of 0.3 m/s.

Experimental results based on 50 trials with the number of cylinder and nonconvex obstacles ranging from 15 to 20 are presented in Table V. It can be seen that for scenarios with cylinder obstacles, NeuPAN improves the success rates by 4.69% and 11.60% compared with RDA and AEMCARL. Moreover, NeuPAN reduces the navigation time by 12.53% and 35.80%, and improves the mobility speed by 5.07% and 12.36%, relative to RDA and AEMCARL respectively. On the other hand, for scenarios with nonconvex obstacles, NeuPAN improves the success rate by 38.19%, reduces the navigation time by 16.33%, and improves the mobility speed by 5.08%, compared to RDA. Note that AEMCARL fails in this situation, since AEMCARL is developed based on the point-mass model (point with inflated radius), which is not applicable to nonconvex obstacles.

It can be seen that none of the simulated schemes achieves 100% success rate. These failures happen due to two reasons. First, the robot’s laser scanner has a limited field of view (FoV), which may fail to detect moving obstacles outside its coverage area. Consequently, the robot might collide with these undetected obstacles before it can react. Second, obstacles are densely packed and moving within a confined area. Their behaviors are randomized and they do not actively avoid the ego robot, as demonstrated in [6]. As a result, there are scenarios where the robot has no viable escape path. For

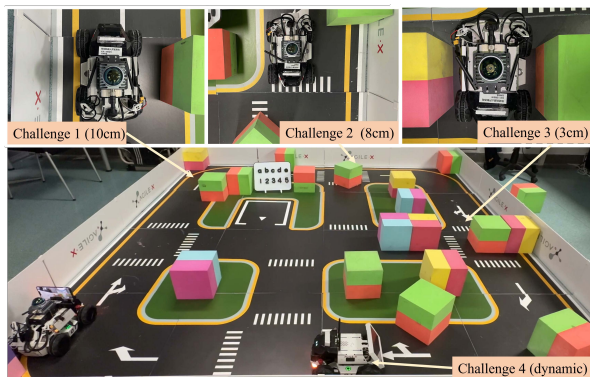
example, if the robot is completely surrounded by obstacles, a collision is inevitable even if the robot remains stationary, as the obstacles would converge toward it.

The robot trajectories and speed profiles of the three schemes are shown in Fig. 11. It can be seen that AEMCARL tends to take detours in front of crowded obstacles due to its conservative neural policy and its over-simplified model treating obstacles as balls, resulting in longer navigation times (Fig. 11(c)). On the other hand, RDA tends to collide with obstacles since it computes inexact robot-obstacle distances based on the polygons converted from laser scans, which introduces inevitable errors in representing nonconvex obstacles, leading to higher failure rates (Fig. 11(f)- 11(g)). Lastly, NeuPAN utilizes the raw points to represent obstacles, which gets rid of the distance errors involved in AEMCARL and RDA. By directly mapping the raw points to actions, NeuPAN achieves better navigation performance in complex environments with arbitrarily-shaped obstacles (Fig. 11(d)- 11(e)).

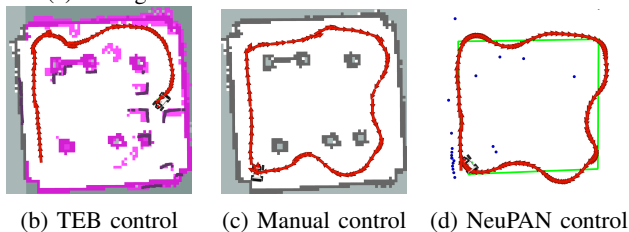
2) *Structured Real-World Testbed*: We conduct the experiments in the structured real-world testbed (i.e., a sandbox with size 4 m×4 m) to demonstrate the high accuracy of NeuPAN, as shown in Fig. 12. The robot is tasked to race within the track as fast as possible without any collision. We set up challenges 1–3 with different DoNs, by varying the positions of 20 cm×20 cm cubes. The narrowest spaces in challenges 1–3 are 32 cm, 30 cm, and 25 cm, respectively. Taking the robot width into account, the remaining margins are 10 cm, 8 cm, 3 cm, respectively, corresponding to the DoN of 0.52, 0.58, 0.79. These challenges represent different passing difficulties and are used to evaluate the limit of navigation accuracy. We

TABLE VI: Performance comparison of NeuPAN, TEB, and manual control in the structured real-world testbed

Scenario	Success			Navigation Time (s)			Moving Speed Mean / std (m/s)		
	NeuPAN	TEB	Manual	NeuPAN	TEB	Manual	NeuPAN	TEB	Manual
Challenge 1 (10cm)	✓	✓	✓	2.87	4.11	4.90			
Challenge 2 (8cm)	✓	✓	✓	6.07	14.99	10.31	0.788	0.265	0.396
Challenge 3 (3cm)	✓	✗	✓	9.25	-	16.98	/ 0.23	/ 0.31	/ 0.165
Challenge 4 (dynamic)	✓	✗	✓	12.49	-	23.95			



(a) Configurations in the structured real-world testbed.



(b) TEB control (c) Manual control (d) NeuPAN control

Fig. 12: Trajectory comparison of TEB, manual, and NeuPAN control in a structured real-world testbed.

also set up challenge 4 with a dynamic obstacle, where we adopt another mobile robot to challenge the ego robot inside the track.

We compare the performance of our approach NeuPAN with the celebrated motion planner TEB [3] and manual control in terms of route completion, navigation time, and average speed. From Fig. 12, it is also observed that the TEB method requires a pre-built occupancy grid map. In contrast, our approach only requires the goal state information, i.e., four checkpoints at the corners. The desired speed is set to be 1 m/s. Quantitative results are listed in Table. VI.

It can be seen that NeuPAN successfully passes all challenges and finishes the track with the shortest time of 12.49 s and highest speed of 0.788 m/s, approaching the maximum speed 1 m/s of the robot. This indicates that NeuPAN achieves a limit of 3 cm control accuracy in this task. In contrast, TEB gets stuck in front of challenge 3 (3 cm-margin passage), failing in completing the trip. This is because TEB relies on occupancy grid maps and the grid representation of obstacles leads to degradation of navigation accuracy, making it inadequate for highly-accurate navigation. By incrementally varying the margin in challenge 3, the TEB method passes challenge 3 at a margin of 7 cm, which represents its navigation accuracy limit. It can be seen that our method improves the accuracy

by over 2x compared to TEB. Lastly, by adopting manual control, it is also possible to control the robot through all these challenges. But due to the need to carefully avoid collision at narrow spaces, manual control leads to longer navigation time (23.95 s) and lower moving speed (0.396 m/s / 0.165), compared to our method. The results corroborate to the effectiveness of our explainable end-to-end framework in the real-world experiment with ubiquitous uncertainties.

3) *Unstructured Real-World Environment*: The above experiments have considered structured environments, where the obstacles are easy to be detected (e.g., box, wall) and classified. However, for extensive real-life applications (e.g., housekeeper machine), the target scenarios are highly unstructured and disordered. To this end, we further test NeuPAN in a highly cluttered laboratory as shown in Fig. 13. The laboratory is filled with sundries, such as chairs, sandboxes, water bottles, and equipment, which are unrecognizable objects with arbitrary shapes. The robot needs to patrol in this environment at a desired speed of 0.5 m/s without a pre-established map. First, we invite 10 human pilots to manually control the robot. But unfortunately, all of them fail, resulting in either robot collisions or time out due to insufficient speed. Then, we adopt NeuPAN to handle this situation. This time, the task is accomplished, with the associated trajectories (marked as blue lines) illustrated in Fig. 13. The narrowest place has only about 3-centimeters tolerance with $\text{DoN} = 0.88$ (see Fig. 13(5)). But owing to the exact distance perception from DUNE and high accurate motion from NRMP, our NeuPAN method is able to navigate the robot through this challenging scenario with only onboard lidar in real time.

The trajectories and speed profiles of NeuPAN and TEB during this task are shown in Fig. 14. We build the occupancy grid map by Cartographer [49], which is a celebrated SLAM algorithm, for TEB to plan its trajectory, as shown in Fig. 14(a). The TEB trajectory (marked in yellow) fails in the narrow space because of the inevitable errors caused by the limited resolution of grid map. Figs. 14(b)-14(d) illustrate the successful trajectory of NeuPAN (marked in blue) and its associated linear and angular speed profiles. It can be seen that the linear speed fluctuates around the target speed 0.5 m/s and the angular speed is rigorously constrained within the range $[-3.14, 3.14]$ rad/s, which achieves a stable and bounded control policy.

D. Experiment 4: Wheel-legged Robot Mapless Navigation

In this subsection, we validate NeuPAN on a medium-size robot platform, i.e., the wheel-legged robot as mentioned in Fig. 1, to conduct autonomous mapless navigation and dense



Fig. 13: Robot navigation in an unstructured cluttered environment. Green straight line is the naive path. Purple points are the raw 2D lidar data. Red line is the optimal receding path. Red points are the input obstacle points. 3D lidar is used for localization. The narrowest space (e.g. (5)) has only about 3-centimeters tolerance with DoN = 0.88.

TABLE VII: Performance comparison of NeuPAN and Falco in the real-world confined space

Narrow Passage	Passable		Navigation Time		Average Move Speed	
	NeuPAN	Falco	NeuPAN	Falco	NeuPAN	Falco
Falco narrow threshold (DoN: 0.79)	✓	✓	9.51	13.56	0.477	0.36
Neupan narrow threshold (DoN: 0.89)	✓	✗	10.15	-	0.468	0.27

mapping tasks in an unknown office building, as illustrated in Fig. 15. The naive path is generated by connecting the straight line between the manually set goal states without consideration of the obstacles in the environment. Fast-lio2 [43] is employed for real-time mapping of the environment and localization of the ego robot. Note that the narrowest space has a DoN value of 0.92. It can be seen from Fig. 15 that there exist 3 challenges between the starting and end points (the same position in Fig. 15(d)): 1) passing a narrow doorway (Fig. 15(a)); 2) avoiding arbitrary obstacles (the potted plant in Fig. 15(b)); 3) circumventing adversarial humans who suddenly rush over to block the way (Fig. 15(c)). Due to the precise actions afforded by NeuPAN, the wheel-legged robot successfully conquers all these challenges. This experiment demonstrates the efficacy and robustness of our approach in enhancing operational capabilities of wheel-legged robots. The changes over time including the trajectory, linear speed, and angular speed, are shown in Fig. 16. It is clear that the wheel-legged robot succeeds in following the goal states and returning to the starting point. The linear speed fluctuates around the desired speed 0.6 m/s, but is rigorously controlled below 1 m/s (the maximum speed requested by the user). Similarly, the angular speed is rigorously controlled between -3.14 rad and $+3.14$ rad. This result show that our approach is constraints guaranteed due to the interpretability and hard-bounded constraints in NRMP block of NeuPAN, which is in contrast to learning-based solutions that may output uncertain motions.

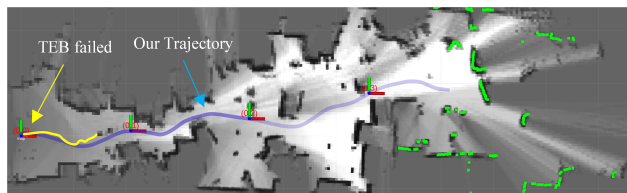
To further demonstrate the effectiveness of our approach operating in the real world, we conduct a quantitative experiment to compare the performance of NeuPAN and Falco [19]. The task is to navigate the wheel-legged robot along a straight

trajectory in a highly-confined space (DoN=0.89), as shown in Fig. 17. It can be seen that NeuPAN successfully navigates the robot through the narrow space, reaching the goal smoothly. In contrast, the Falco method gets stuck in front of the narrow passage. This is because Falco converts the lidar points into voxels for collision avoidance and determines the trajectories by maximizing the probability to reach the goal. The point voxelization and probabilistic sampling operations result in degradation of navigation accuracy. Quantitative results are shown in Table VII. It can be seen that NeuPAN improves the DoN (i.e., navigation accuracy) from 0.79 to 0.89, corresponding to over 12.6% DoN gain and 2x accuracy improvement compared with Falco. Furthermore, compared to Falco under the same challenge (DoN=0.79), NeuPAN achieves higher moving speed (32.5% improvement) and shorter navigation time (29.9% reduction).

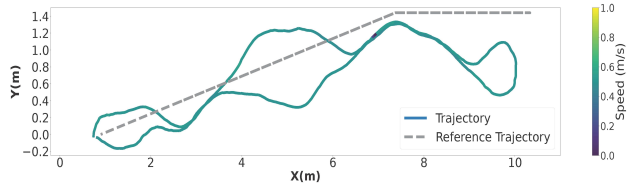
E. Experiment 5: Passenger Vehicle Navigation

In this subsection, we validate NeuPAN on a large-size passenger vehicle platform. Compared to the aforementioned robots, the vehicle has a larger value of speed (e.g., 10 to 50 km/h) and minimum turning radius (i.e., 6 m). Therefore, existing solutions for passenger vehicles adopt a larger safety distance (e.g. 1 m), and vehicles often stop in front of confined spaces. In the following experiments, we will show that NeuPAN can overcome the above drawbacks.

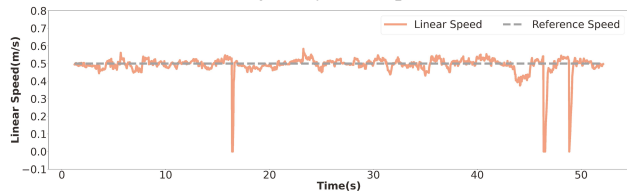
1) *Simulated Environment*: We employ CARLA [50], a high-fidelity simulator powered by unreal engine, to create a virtual parking lot scenario in Fig. 18. A 128-line 3D lidar mounted on top of the vehicle provides real-time measurements of the environment. The task is to navigate the vehicle



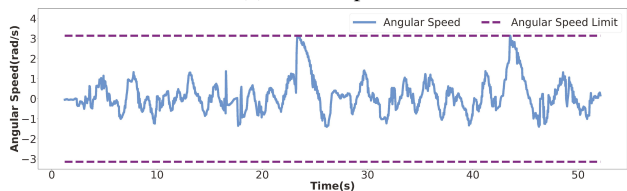
(a) Trajectories in the grip map.



(b) Trajectory with speed.

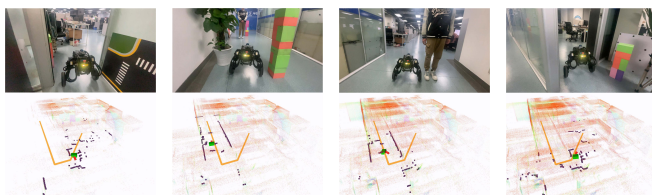


(c) Linear speed



(d) Angular speed

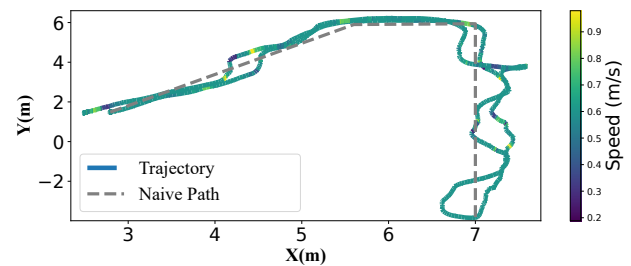
Fig. 14: Trajectory, linear, and angular speed profiles of the agile mobile robot during the office navigation task.



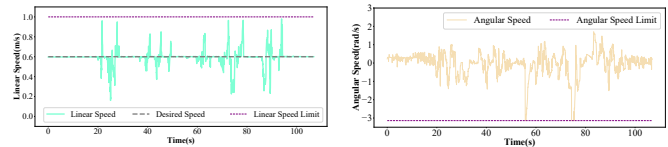
(a) Doorway. (b) Gap. (c) Blocker. (d) Return.

Fig. 15: Wheel-legged mapless navigation in the office.

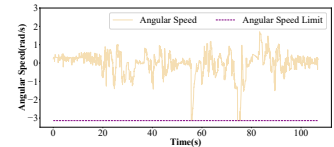
from zone A to zone B, and consists of two phases. In the first phase, as shown in Fig. 18(c), illegally parked vehicles block the way with $\text{DoN} = 0.95$. But due to the end-to-end feature, NeuPAN successfully finds the optimal actions under the kinematics constraints in real time, and the successful trajectory is shown in Figs. 18(a)-18(c). In the second phase, as shown in Figs. 18(d)-18(f), an adversarial dynamic traffic flow is generated to simulate the real world adversarial or even accidental traffics. For instance, in Fig. 18(e), a dangerous obstacle vehicle crash into our ego vehicle. After the crash moment, NeuPAN generates an expert-driver-like steering and accelerating action, which rehabilitates the vehicle from a crash and makes a timely turn. Figs. 18(g)-18(i) illustrate other challenging cases under the dynamic traffic flows. In-



(a) Trajectory with linear speed change.



(b) Linear speed



(c) Angular speed

Fig. 16: Trajectory, linear, and angular speed change of the wheel-legged robot during the mapless navigation task.

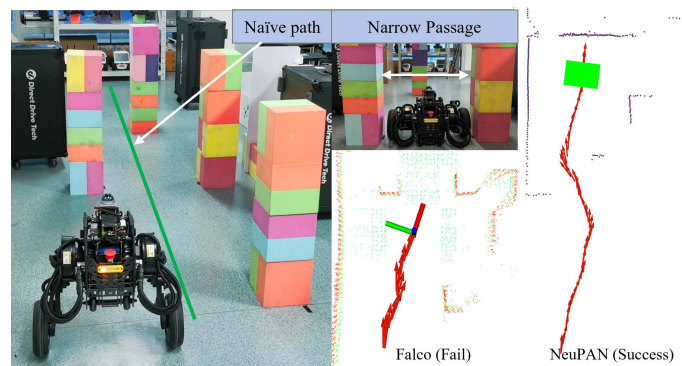


Fig. 17: Trajectory comparison of NeuPAN and Falco in the real-world confined space.

terestingly, Fig 18(h) presents an extreme case where the gap is too narrow for any existing methods to pass. This is because the detected boxes are slightly bigger than the actual objects, making the width of the remaining drivable area smaller than the width of ego vehicle. However, our methodology makes impassable passable, by maneuvering the vehicle pass through this challenging case successfully, as shown in Fig 18(h). This already exceeds human-level driving, as tested by our volunteer human drivers.

2) *Real World Environment*: In existing works, numerous methodologies, such as end-to-end RL, have demonstrated great potential in simulated environments. Nevertheless, these approaches face difficulties when applied to real-world scenarios due to the sim-to-real gap. Real-world testing can also verify the robustness of NeuPAN since hardware uncertainties (e.g., noises, impairments) are now considered.

First, we test the vehicle with a 128-line lidar in the parking lot, as shown in Fig. 19. Unlike the wide-open environment on the road, the parking lot leaves less space for the vehicle to pass ($\text{DoN}=0.93$). Existing solutions that adopt object detection or occupancy grids are prone to take a detour or get stuck. In contrast, NeuPAN successfully controls the vehicle to move with an S-shaped trajectory to avoid boxes and mannequins as

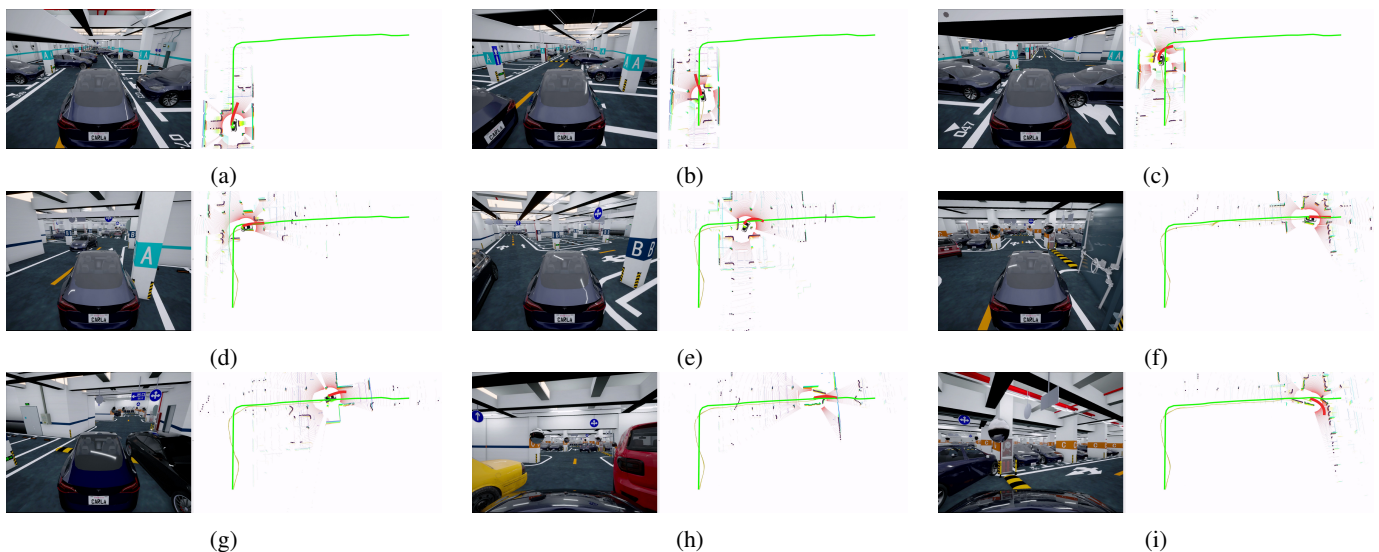


Fig. 18: Passenger vehicle navigation in Carla. (a)–(c): Illegally parked vehicles block the road, leaving only a narrow passable space (DoN = 0.97). (d)–(f): Randomly generated traffic flow. (g)–(i): Challenging cases in the traffic flow.

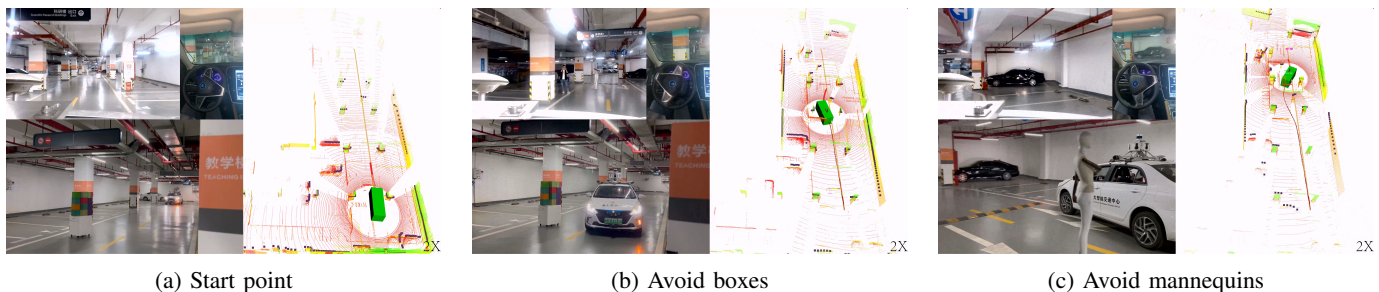


Fig. 19: The real-world experiment of passenger vehicle navigation in the parking lot with boxes, mannequins, and other vehicles.

illustrated in Figs. 19(a)–19(c).

Second, we conduct a simple yet specially designed experiment to validate the performance of NeuPAN. In this challenge, the vehicle needs to pass an extremely narrow passage with a width of 1.82 m within a certain time budget (corresponding to an average speed of 5 km/h). As the vehicle width is already 1.77 m, there is only about 5 centimeters tolerance (DoN=0.97). We compare our NeuPAN with: 1) hybrid A star implemented by Autoware [51], [52], a state-of-the-art open-source autonomous driving solution, and 2) human driving. First, it can be seen that even under a DoN close to 1, our NeuPAN solution successfully navigates the vehicle through the gap at a speed of 7 km/h, as shown in Fig. 20(a). Second, the human driver is very likely to fail given a speed of 5 km/h. Only when we reduce the speed to a lower value (e.g. 2 km/h) can the human driver tackle this situation by careful observations, as shown in Fig 20(b). Lastly, the Autoware solution, i.e., hybrid A star, converts the lidar scans into occupancy grids, as shown in Fig. 20(c). This approach treats the narrow gap as impassable, thereby generating alternative directions for detouring. In contrast, our NeuPAN solution directly utilizes the lidar points as input, achieving higher accuracy and successfully finding the optimal

path, as illustrated in Fig. 20(d). The above experiments demonstrate the advantage of the proposed framework in extremely cluttered environments. This advantage makes our approach very promising in handling various difficult cases.

VII. CONCLUSION

This article proposes NeuPAN, an end-to-end model-based learning approach for direct point robot navigation. A novel tightly-coupled perception-to-control framework, including DUNE and NRMP, is developed to directly map the raw points to the robot actions without error propagation. Owing to the interpretable deep unfolding neural network, DUNE can be trained in a sim-to-real fashion to convert obstacle points to latent distance features rapidly. The output distance features are embedded as neural regularizers to generate collision-free and time-efficient robot actions by NRMP, represented by differentiable convex optimization layers. Exhaustive experiments on multiple robot platforms in diverse scenarios are conducted to validate NeuPAN, which show that NeuPAN outperforms existing state-of-the-art approaches with over 2x accuracy improvement, reduced navigation time, higher average speed, better robustness and generalization capabilities. Since NeuPAN generates perception-aware and physically interpretable motions in the real-time, it empowers autonomous

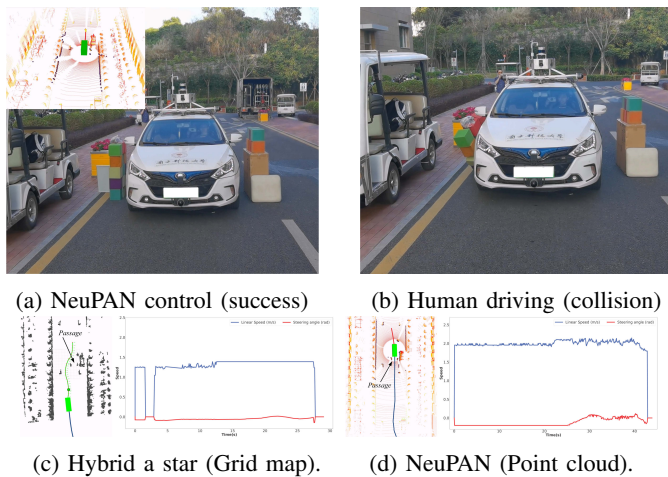


Fig. 20: Real-world experiment of passenger vehicle navigation through a narrow passage (DoN = 0.97). (a) NeuPAN succeeds at 7 km/h. (b) Human driver fails at 5 km/h. (c) The trajectory, linear speed, and steering angle of the Hybrid A star guided passenger vehicle. (d) The trajectory, linear speed and steering angle of the NeuPAN guided passenger vehicle.

systems to work in cluttered environments that are previously considered impassable, triggering new applications such as cluttered-room housekeeping and limited-space operating.

REFERENCES

- [1] X. Zhang, A. Liniger, and F. Borrelli, "Optimization-based collision avoidance," *IEEE Transactions on Control Systems Technology*, vol. 29, no. 3, pp. 972–983, 2020.
- [2] S. Kousik, B. Zhang, P. Zhao, and R. Vasudevan, "Safe, optimal, real-time trajectory planning with a parallel constrained bernstein algorithm," *IEEE Transactions on Robotics*, vol. 37, no. 3, pp. 815–830, 2020.
- [3] C. Rösmann, F. Hoffmann, and T. Bertram, "Kinodynamic trajectory optimization and control for car-like robots," in *2017 IEEE/RSJ International Conference on Intelligent Robots and Systems (IROS)*. IEEE, 2017, pp. 5681–5686.
- [4] B. Zhou, J. Pan, F. Gao, and S. Shen, "Raptor: Robust and perception-aware trajectory replanning for quadrotor fast flight," *IEEE Transactions on Robotics*, vol. 37, no. 6, pp. 1992–2009, 2021.
- [5] R. Han, S. Chen, S. Wang, Z. Zhang, R. Gao, Q. Hao, and J. Pan, "Reinforcement learned distributed multi-robot navigation with reciprocal velocity obstacle shaped rewards," *IEEE Robotics and Automation Letters*, vol. 7, no. 3, pp. 5896–5903, 2022.
- [6] C. Chen, Y. Liu, S. Kreiss, and A. Alahi, "Crowd-robot interaction: Crowd-aware robot navigation with attention-based deep reinforcement learning," in *2019 International Conference on Robotics and Automation (ICRA)*. IEEE, 2019, pp. 6015–6022.
- [7] T. Fan, P. Long, W. Liu, and J. Pan, "Distributed multi-robot collision avoidance via deep reinforcement learning for navigation in complex scenarios," *The International Journal of Robotics Research*, vol. 39, no. 7, pp. 856–892, 2020.
- [8] R. Han, S. Chen, and Q. Hao, "Cooperative multi-robot navigation in dynamic environment with deep reinforcement learning," in *2020 IEEE International Conference on Robotics and Automation (ICRA)*. IEEE, 2020, pp. 448–454.
- [9] J. Tordesillas, B. T. Lopez, M. Everett, and J. P. How, "Faster: Fast and safe trajectory planner for navigation in unknown environments," *IEEE Transactions on Robotics*, vol. 38, no. 2, pp. 922–938, 2021.
- [10] Z. Zhang, Y. Zhang, R. Han, L. Zhang, and J. Pan, "A generalized continuous collision detection framework of polynomial trajectory for mobile robots in cluttered environments," *IEEE Robotics and Automation Letters*, vol. 7, no. 4, pp. 9810–9817, 2022.
- [11] A. Devo, G. Mezzetti, G. Costante, M. L. Fravolini, and P. Valigi, "Towards generalization in target-driven visual navigation by using deep reinforcement learning," *IEEE Transactions on Robotics*, vol. 36, no. 5, pp. 1546–1561, 2020.
- [12] W. Xiao, T.-H. Wang, R. Hasani, M. Chahine, A. Amini, X. Li, and D. Rus, "Barriernet: Differentiable control barrier functions for learning of safe robot control," *IEEE Transactions on Robotics*, 2023.
- [13] Y. Hu, J. Yang, L. Chen, K. Li, C. Sima, X. Zhu, S. Chai, S. Du, T. Lin, W. Wang *et al.*, "Planning-oriented autonomous driving," in *Proceedings of the IEEE/CVF Conference on Computer Vision and Pattern Recognition*, 2023, pp. 17 853–17 862.
- [14] Z. Li, W. Wang, H. Li, E. Xie, C. Sima, T. Lu, Y. Qiao, and J. Dai, "Befvformer: Learning bird's-eye-view representation from multi-camera images via spatiotemporal transformers," in *European Conference on Computer Vision*. Springer, 2022, pp. 1–18.
- [15] L. Mescheder, M. Oechsle, M. Niemeyer, S. Nowozin, and A. Geiger, "Occupancy networks: Learning 3d reconstruction in function space," in *Proceedings of the IEEE/CVF Conference on Computer Vision and Pattern Recognition*, 2019, pp. 4460–4470.
- [16] A. H. Qureshi, Y. Miao, A. Simeonov, and M. C. Yip, "Motion planning networks: Bridging the gap between learning-based and classical motion planners," *IEEE Transactions on Robotics*, vol. 37, no. 1, pp. 48–66, 2020.
- [17] M. Montemerlo, J. Becker, S. Bhat, H. Dahlkamp, D. Dolgov, S. Ettinger, D. Haehnel, T. Hilden, G. Hoffmann, B. Huhnke *et al.*, "Junior: The stanford entry in the urban challenge," *Journal of field Robotics*, vol. 25, no. 9, pp. 569–597, 2008.
- [18] O. Salzman and D. Halperin, "Asymptotically near-optimal rrt for fast, high-quality motion planning," *IEEE Transactions on Robotics*, vol. 32, no. 3, pp. 473–483, 2016.
- [19] J. Zhang, C. Hu, R. G. Chadha, and S. Singh, "Falco: Fast likelihood-based collision avoidance with extension to human-guided navigation," *Journal of Field Robotics*, vol. 37, no. 8, pp. 1300–1313, 2020.
- [20] R. Han, S. Wang, S. Wang, Z. Zhang, Q. Zhang, Y. C. Eldar, Q. Hao, and J. Pan, "Rda: An accelerated collision free motion planner for autonomous navigation in cluttered environments," *IEEE Robotics and Automation Letters*, vol. 8, no. 3, pp. 1715–1722, 2023.
- [21] W. Ding, L. Zhang, J. Chen, and S. Shen, "Epsilon: An efficient planning system for automated vehicles in highly interactive environments," *IEEE Transactions on Robotics*, vol. 38, no. 2, pp. 1118–1138, 2021.
- [22] Z. Han, Y. Wu, T. Li, L. Zhang, L. Pei, L. Xu, C. Li, C. Ma, C. Xu, S. Shen *et al.*, "An efficient spatial-temporal trajectory planner for autonomous vehicles in unstructured environments," *IEEE Transactions on Intelligent Transportation Systems*, 2023.
- [23] X. Zhou, Z. Wang, H. Ye, C. Xu, and F. Gao, "Ego-planner: An esdf-free gradient-based local planner for quadrotors," *IEEE Robotics and Automation Letters*, vol. 6, no. 2, pp. 478–485, 2020.
- [24] S. Wang, R. Gao, R. Han, S. Chen, C. Li, and Q. Hao, "Adaptive environment modeling based reinforcement learning for collision avoidance in complex scenes," in *2022 IEEE/RSJ International Conference on Intelligent Robots and Systems (IROS)*. IEEE, 2022, pp. 9011–9018.
- [25] L. Li, Y. Miao, A. H. Qureshi, and M. C. Yip, "Mpc-mpnet: Model-predictive motion planning networks for fast, near-optimal planning under kinodynamic constraints," *IEEE Robotics and Automation Letters*, vol. 6, no. 3, pp. 4496–4503, 2021.
- [26] A. Tampuu, T. Matiisen, M. Semikin, D. Fishman, and N. Muhammad, "A survey of end-to-end driving: Architectures and training methods," *IEEE Transactions on Neural Networks and Learning Systems*, vol. 33, no. 4, pp. 1364–1384, 2020.
- [27] A. Francis, A. Faust, H.-T. L. Chiang, J. Hsu, J. C. Kew, M. Fiser, and T.-W. E. Lee, "Long-range indoor navigation with prm-rl," *IEEE Transactions on Robotics*, vol. 36, no. 4, pp. 1115–1134, 2020.
- [28] Y. F. Chen, M. Liu, M. Everett, and J. P. How, "Decentralized non-communicating multiagent collision avoidance with deep reinforcement learning," in *2017 IEEE International Conference on Robotics and Automation (ICRA)*. IEEE, 2017, pp. 285–292.
- [29] M. Everett, Y. F. Chen, and J. P. How, "Motion planning among dynamic, decision-making agents with deep reinforcement learning," in *2018 IEEE/RSJ International Conference on Intelligent Robots and Systems (IROS)*. IEEE, 2018, pp. 3052–3059.
- [30] C. Chen, S. Hu, P. Nikdel, G. Mori, and M. Savva, "Relational graph learning for crowd navigation," in *2020 IEEE/RSJ International Conference on Intelligent Robots and Systems (IROS)*. IEEE, 2020, pp. 10 007–10 013.
- [31] J. Lin, L. Wang, F. Gao, S. Shen, and F. Zhang, "Flying through a narrow gap using neural network: an end-to-end planning and control approach,"

- in *2019 IEEE/RSJ International Conference on Intelligent Robots and Systems (IROS)*. IEEE, 2019, pp. 3526–3533.
- [32] T. Salzmann, E. Kaufmann, J. Arrizabalaga, M. Pavone, D. Scaramuzza, and M. Ryll, “Real-time neural mpc: Deep learning model predictive control for quadrotors and agile robotic platforms,” *IEEE Robotics and Automation Letters*, vol. 8, no. 4, pp. 2397–2404, 2023.
- [33] J. Sacks and B. Boots, “Learning sampling distributions for model predictive control,” in *Conference on Robot Learning*. PMLR, 2023, pp. 1733–1742.
- [34] G. Williams, P. Drews, B. Goldfain, J. M. Rehg, and E. A. Theodorou, “Information-theoretic model predictive control: Theory and applications to autonomous driving,” *IEEE Transactions on Robotics*, vol. 34, no. 6, pp. 1603–1622, 2018.
- [35] B. Amos, I. Jimenez, J. Sacks, B. Boots, and J. Z. Kolter, “Differentiable mpc for end-to-end planning and control,” *Advances in Neural Information Processing Systems*, vol. 31, 2018.
- [36] A. Agrawal, S. Barratt, and S. Boyd, “Learning convex optimization models,” *IEEE/CAA Journal of Automatica Sinica*, vol. 8, no. 8, pp. 1355–1364, 2021.
- [37] S. P. Boyd and L. Vandenberghe, *Convex optimization*. Cambridge university press, 2004.
- [38] J. Schulman, Y. Duan, J. Ho, A. Lee, I. Awwal, H. Bradlow, J. Pan, S. Patil, K. Goldberg, and P. Abbeel, “Motion planning with sequential convex optimization and convex collision checking,” *The International Journal of Robotics Research*, vol. 33, no. 9, pp. 1251–1270, 2014.
- [39] Z. Liu, A. Amini, S. Zhu, S. Karaman, S. Han, and D. L. Rus, “Efficient and robust lidar-based end-to-end navigation,” in *2021 IEEE International Conference on Robotics and Automation (ICRA)*. IEEE, 2021, pp. 13 247–13 254.
- [40] A. Domahidi, E. Chu, and S. Boyd, “ECOS: An SOCP solver for embedded systems,” in *European Control Conference (ECC)*, 2013, pp. 3071–3076.
- [41] Y. Yang, M. Pesavento, Z.-Q. Luo, and B. Ottersten, “Inexact block coordinate descent algorithms for nonsmooth nonconvex optimization,” *IEEE Transactions on Signal Processing*, vol. 68, pp. 947–961, 2019.
- [42] A. Agrawal, B. Amos, S. Barratt, S. Boyd, S. Diamond, and J. Z. Kolter, “Differentiable convex optimization layers,” *Advances in Neural Information Processing systems*, vol. 32, 2019.
- [43] W. Xu, Y. Cai, D. He, J. Lin, and F. Zhang, “Fast-lid2: Fast direct lidar-inertial odometry,” *IEEE Transactions on Robotics*, vol. 38, no. 4, pp. 2053–2073, 2022.
- [44] T. Shan and B. Englot, “Lego-loam: Lightweight and ground-optimized lidar odometry and mapping on variable terrain,” in *2018 IEEE/RSJ International Conference on Intelligent Robots and Systems (IROS)*. IEEE, 2018, pp. 4758–4765.
- [45] G. Kim and A. Kim, “Scan context: Egocentric spatial descriptor for place recognition within 3D point cloud map,” in *Proceedings of the IEEE/RSJ International Conference on Intelligent Robots and Systems*, Madrid, Oct. 2018.
- [46] A. Geiger, P. Lenz, and R. Urtasun, “Are we ready for autonomous driving? the kitti vision benchmark suite,” in *Conference on Computer Vision and Pattern Recognition (CVPR)*, 2012.
- [47] A. H. Lang, S. Vora, H. Caesar, L. Zhou, J. Yang, and O. Beijbom, “Pointpillars: Fast encoders for object detection from point clouds,” in *Proceedings of the IEEE/CVF Conference on Computer Vision and Pattern Recognition*, 2019, pp. 12 697–12 705.
- [48] N. Koenig and A. Howard, “Design and use paradigms for gazebo, an open-source multi-robot simulator,” in *2004 IEEE/RSJ International Conference on Intelligent Robots and Systems (IROS)(IEEE Cat. No. 04CH37566)*, vol. 3. IEEE, 2004, pp. 2149–2154.
- [49] W. Hess, D. Kohler, H. Rapp, and D. Andor, “Real-time loop closure in 2d lidar slam,” in *2016 IEEE International Conference on Robotics and Automation (ICRA)*. IEEE, 2016, pp. 1271–1278.
- [50] A. Dosovitskiy, G. Ros, F. Codevilla, A. Lopez, and V. Koltun, “Carla: An open urban driving simulator,” in *Conference on Robot Learning*. PMLR, 2017, pp. 1–16.
- [51] K. Kurzer, “Path planning in unstructured environments: A real-time hybrid a* implementation for fast and deterministic path generation for the kth research concept vehicle,” 2016.
- [52] S. Kato, S. Tokunaga, Y. Maruyama, S. Maeda, M. Hirabayashi, Y. Kitsukawa, A. Monroy, T. Ando, Y. Fujii, and T. Azumi, “Autoware on board: Enabling autonomous vehicles with embedded systems,” in *2018 ACM/IEEE 9th International Conference on Cyber-Physical Systems (ICCPs)*. IEEE, 2018, pp. 287–296.
- [53] K. M. Lynch and F. C. Park, *Modern Robotics*. Cambridge University Press, 2017.
- [54] J. Bolte, S. Sabach, and M. Teboulle, “Proximal alternating linearized minimization for nonconvex and nonsmooth problems,” *Mathematical Programming*, vol. 146, pp. 459–494, 2014.

APPENDIX A

ACKERMANN AND DIFFERENTIAL MODELS

Car-like robots adhere to the Ackermann model has the nonlinear kinematic function [53]:

$$f(\mathbf{s}_t, \mathbf{u}_t) = \left[v_t \cos(\theta_t), v_t \sin(\theta_t), \frac{v_t \tan \psi_t}{L} \right]^T,$$

where v_t and ψ_t are the linear speed and steering angle of the robot at time t , respectively. L is the wheelbase. θ_t is the orientation of the robot. This non-linear function can be linearized into the structure of Eq. (2) by the first-order Taylor polynomial, where the associated coefficients (\mathbf{A}_t , \mathbf{B}_t , \mathbf{c}_t) at time t in Eq. (2) are given by:

$$\begin{aligned} \mathbf{A}_t &= \begin{bmatrix} 1 & 0 & -\bar{v}_t \sin(\bar{\theta}_t) \Delta t \\ 0 & 1 & \bar{v}_t \cos(\bar{\theta}_t) \Delta t \\ 0 & 0 & 1 \end{bmatrix}, \\ \mathbf{B}_t &= \begin{bmatrix} \cos(\bar{\theta}_t) \Delta t & 0 \\ \sin(\bar{\theta}_t) \Delta t & 0 \\ \frac{\tan \bar{\psi}_t \Delta t}{L} & \frac{\bar{v}_t \Delta t}{L \cos^2 \bar{\psi}_t} \end{bmatrix}, \\ \mathbf{c}_t &= \begin{bmatrix} \bar{\theta}_t \bar{v}_t \sin(\bar{\theta}_t) \Delta t \\ -\bar{\theta}_t \bar{v}_t \cos(\bar{\theta}_t) \Delta t \\ -\frac{\bar{\psi}_t \bar{v}_t \Delta t}{L \cos^2 \bar{\psi}_t} \end{bmatrix}, \end{aligned} \quad (35)$$

where \bar{v}_t and $\bar{\psi}_t$ are the nominal linear speed and steering angle of the control vector $\bar{\mathbf{u}}_t$ at time t , respectively. Similarly, the differential drive robots with the control vector: linear velocity v_t and angular velocity ω_t have the kinematic function $f(\mathbf{s}_t, \mathbf{u}_t) = [v_t \cos(\theta_t), v_t \sin(\theta_t), \omega_t]^T$, can be modeled to be a linear form by the following coefficients:

$$\begin{aligned} \mathbf{A}_t &= \begin{bmatrix} 1 & 0 & -\bar{v}_t \sin(\bar{\theta}_t) \Delta t \\ 0 & 1 & \bar{v}_t \cos(\bar{\theta}_t) \Delta t \\ 0 & 0 & 1 \end{bmatrix}, \\ \mathbf{B}_t &= \begin{bmatrix} \cos(\bar{\theta}_t) \Delta t & 0 \\ \sin(\bar{\theta}_t) \Delta t & 0 \\ 0 & \Delta t \end{bmatrix}, \\ \mathbf{c}_t &= \begin{bmatrix} \bar{\theta}_t \bar{v}_t \sin(\bar{\theta}_t) \Delta t \\ -\bar{\theta}_t \bar{v}_t \cos(\bar{\theta}_t) \Delta t \\ 0 \end{bmatrix}, \end{aligned} \quad (36)$$

APPENDIX B

EQUIVALENCE BETWEEN P AND Q

To prove this, we substitute $D_{i,t}$ into $\text{dist}(\mathbb{Z}_t(\mathbf{s}_t), \mathbb{P}_t)$ in Eq. (7). Then, the constraint Eq. (11b) in P is equivalent to

$$\text{dist}(\mathbb{Z}_t(\mathbf{s}_t), \mathbb{P}_t; \{\boldsymbol{\mu}_t^i, \boldsymbol{\lambda}_t^i\}) \geq d_{\min} \iff$$

$$\min_{i=1, \dots, M} \left\{ \boldsymbol{\lambda}_t^{i \top} [\mathbf{t}_t(\mathbf{s}_t) - \mathbf{p}_t^i] - \boldsymbol{\mu}_t^{i \top} \mathbf{h} \right\} \geq d_{\min}, \quad (37a)$$

$$\boldsymbol{\mu}_t^{i \top} \mathbf{G} + \boldsymbol{\lambda}_t^{i \top} \mathbf{R}(\mathbf{s}_t) = \mathbf{0}, \quad (37b)$$

$$\{\boldsymbol{\mu}_t^i, \boldsymbol{\lambda}_t^i\} \in \mathcal{G}. \quad (37c)$$

Based on the definitions of I in Eq. (14) and E in Eq. (15), constraints Eq. (37a) and Eq. (37b) are equivalently re-written as

$$\min \{I(\mathbf{s}_t, \boldsymbol{\mu}_t^i, \boldsymbol{\lambda}_t^i), 0\} = 0, \quad E(\mathbf{s}_t, \boldsymbol{\mu}_t^i, \boldsymbol{\lambda}_t^i) = 0. \quad (38)$$

According to the penalty theory, the equality constraints Eq. (38) can be removed and automatically satisfied by adding penalty terms $\|\min(I, 0)\|_2^2 + \|E\|_2^2$ for all (i, t) to the objective of P. Then problem P is equivalently transformed into Q.

APPENDIX C PROOF OF THEOREM 1

To prove the theorem, we first define $\mathcal{X} = \{\mathcal{S}, \mathcal{U}\}$ and $\mathcal{Y} = \{\mathcal{M}, \mathcal{L}\}$. Let $f(\mathcal{X}) = C_0(\mathcal{S}, \mathcal{U}) + \mathbb{I}_{\mathcal{F}}(\mathcal{S}, \mathcal{U})$ and $g(\mathcal{Y}) = \mathbb{I}_{\mathcal{G}}(\mathcal{S}, \mathcal{U})$, where $\mathbb{I}_{\mathcal{F}}, \mathbb{I}_{\mathcal{G}}$ are indicator functions for the feasible sets \mathcal{F}, \mathcal{G} . Then problem Q is equivalently written as

$$\text{M} : \min_{\mathcal{X}, \mathcal{Y}} \underbrace{f(\mathcal{X}) + g(\mathcal{Y}) + C_r(\mathcal{X}, \mathcal{Y})}_{:=\Psi(\mathcal{X}, \mathcal{Y})} \quad (39)$$

It can be seen that Ψ is an extended proper and lower semicontinuous function of C_{e2e} , by incorporating constraints as indicator functions into C_{e2e} , and C_r is a continuous C^1 function. Based on Sections IV and V, it is clear that NeuPAN is equivalent to the following alternating discrete dynamical system in the form of $\mathcal{X}^{[k]}, \mathcal{Y}^{[k]} \rightarrow \mathcal{X}^{[k+1]}, \mathcal{Y}^{[k+1]} \rightarrow \mathcal{X}^{[k+2]}, \mathcal{Y}^{[k+2]}$ (given the initial $\mathcal{X}^{[0]}, \mathcal{Y}^{[0]}$):

$$\mathcal{Y}^{[k+1]} = \underset{\mathcal{Y}}{\operatorname{argmin}} \left\{ \widehat{\Psi}(\mathcal{X}^{[k]}, \mathcal{Y}) \right\}, \quad (\text{DUNE}), \quad (40a)$$

$$\mathcal{X}^{[k+1]} = \underset{\mathcal{X}}{\operatorname{argmin}} \left\{ \Psi(\mathcal{X}, \mathcal{Y}^{[k+1]}) + \frac{b_k}{2} \|\mathbf{x} - \mathbf{x}^{[k]}\|_2^2 \right\}, \quad (\text{NRMP}), \quad (40b)$$

where $\mathbf{x} = \operatorname{vec}(\mathcal{X})$ and $\mathbf{y} = \operatorname{vec}(\mathcal{Y})$ are vectorization of sets \mathcal{X}, \mathcal{Y} , and $\{b_k\}$ are positive real numbers. The function $\widehat{\Psi} = f + g + \widehat{C}_r$, where \widehat{C}_r is an universal approximate of C_r with the differences between their function values and gradients bounded as

$$\|\partial C_r(\mathcal{X}, \mathcal{Y}) - \partial \widehat{C}_r(\mathcal{X}, \mathcal{Y})\|_2 \leq \epsilon, \quad (41a)$$

$$\|C_r(\mathcal{X}, \mathcal{Y}) - \widehat{C}_r(\mathcal{X}, \mathcal{Y})\|_2 \leq \epsilon, \quad (41b)$$

where $\epsilon \rightarrow 0$ as the number of layers of DUNE goes to infinity.

A. Proof of Part (i)

With the above notations and assumptions, we now prove part (i). First, substituting $\mathcal{Y}^{[k+1]}$ and $\mathcal{Y}^{[k]}$ into Eq. (40a), we have

$$\widehat{\Psi}(\{\mathcal{X}^{[k]}, \mathcal{Y}^{[k]}\}) \geq \widehat{\Psi}(\{\mathcal{X}^{[k]}, \mathcal{Y}^{[k+1]}\}). \quad (42)$$

Putting $\mathcal{X}^{[k+1]}$ and $\mathcal{X}^{[k]}$ into Eq. (40b), we have

$$\Psi(\{\mathcal{X}^{[k]}, \mathcal{Y}^{[k+1]}\}) \geq \Psi(\{\mathcal{X}^{[k+1]}, \mathcal{Y}^{[k+1]}\}) + \frac{b_k}{2} \|\mathbf{x}^{[k+1]} - \mathbf{x}^{[k]}\|_2^2. \quad (43)$$

Combining the above two equations Eq. (42)Eq. (43) leads to

$$\Psi(\{\mathcal{X}^{[k]}, \mathcal{Y}^{[k]}\}) - \Psi(\{\mathcal{X}^{[k+1]}, \mathcal{Y}^{[k+1]}\}) \geq \frac{b_k}{2} \|\mathbf{x}^{[k+1]} - \mathbf{x}^{[k]}\|_2^2 - \frac{\widehat{L}_2 + L_2}{2} \|\mathbf{y}^{[k+1]} - \mathbf{y}^{[k]}\|_2^2, \quad (44)$$

where L_2 and \widehat{L}_2 are Lipschitz constants of C_r and \widehat{C}_r , respectively. Since C_0 and C_r are norm functions, it is clear that L_2 and \widehat{L}_2 are finite numbers. Now we consider two cases.

- $\|\mathbf{x}^{[k+1]} - \mathbf{x}^{[k]}\|_2 \neq 0$. In this case, there always exists some b_k such that $b_k > (\widehat{L}_2 + L_2) \frac{\|\mathbf{y}^{[k+1]} - \mathbf{y}^{[k]}\|_2^2}{\|\mathbf{x}^{[k+1]} - \mathbf{x}^{[k]}\|_2^2}$. By setting

$$\varrho = \left[b_k - (\widehat{L}_2 + L_2) \frac{\|\mathbf{y}^{[k+1]} - \mathbf{y}^{[k]}\|_2^2}{\|\mathbf{x}^{[k+1]} - \mathbf{x}^{[k]}\|_2^2} \right] \times \left(1 + \frac{\|\mathbf{y}^{[k+1]} - \mathbf{y}^{[k]}\|_2^2}{\|\mathbf{x}^{[k+1]} - \mathbf{x}^{[k]}\|_2^2} \right)^{-1} > 0, \quad (45)$$

we obtain

$$\Psi(\{\mathcal{X}^{[k]}, \mathcal{Y}^{[k]}\}) - \Psi(\{\mathcal{X}^{[k+1]}, \mathcal{Y}^{[k+1]}\}) \geq \frac{\varrho}{2} \left[\|\mathbf{x}^{[k+1]} - \mathbf{x}^{[k]}\|_2^2 + \|\mathbf{y}^{[k+1]} - \mathbf{y}^{[k]}\|_2^2 \right]. \quad (46)$$

- $\|\mathbf{x}^{[k+1]} - \mathbf{x}^{[k]}\|_2 = 0$. In this case, $\|\mathbf{y}^{[k+1]} - \mathbf{y}^{[k]}\|_2 = 0$ must hold. This is because $\mathbf{y} = \operatorname{vec}(\mathcal{Y}) = \operatorname{vec}(\{\mathcal{M}, \mathcal{L}\})$ represents point-to-shape distance, and is uniquely defined by the robot state \mathbf{x} . The distances associated with two equivalent robot states are guaranteed to be the same. This is exactly why we can abandon proximal terms in DUNE. This implies that Eq. (46) also holds.

Combining the above two cases, the proof for part (i) is completed.

B. Proof of Part (ii)

To prove part (ii), we sum up Eq. (46) from $k = 0$ to $N - 1$, where N is a positive integer, and obtain

$$\sum_{k=0}^{N-1} \left(\|\mathbf{x}^{[k+1]} - \mathbf{x}^{[k]}\|_2^2 + \|\mathbf{y}^{[k+1]} - \mathbf{y}^{[k]}\|_2^2 \right) \leq \frac{2}{\varrho} \left[\Psi(\mathcal{X}^{[0]}, \mathcal{Y}^{[0]}) - \Psi(\mathcal{X}^{[N]}, \mathcal{Y}^{[N]}) \right]. \quad (47)$$

Taking $N \rightarrow \infty$, we have

$$\sum_{k=0}^{\infty} \left(\|\mathbf{x}^{[k+1]} - \mathbf{x}^{[k]}\|_2^2 + \|\mathbf{y}^{[k+1]} - \mathbf{y}^{[k]}\|_2^2 \right) < \infty, \quad (48)$$

which gives $\lim_{k \rightarrow \infty} \|\mathbf{x}^{[k+1]} - \mathbf{x}^{[k]}\|_2 \rightarrow 0$.

C. Proof of Part (iii)

To prove part (iii), we first take the sub-differential on both sides of Eq. (40a)Eq. (40b), which yields

$$\partial_{\mathbf{y}} \widehat{\Psi}(\mathbf{x}^{[k]}, \mathbf{y}^{[k+1]}) + c_k(\mathbf{y}^{[k+1]} - \mathbf{y}^{[k]}) = 0, \quad (49a)$$

$$\partial_{\mathbf{x}} \Psi(\mathbf{x}^{[k+1]}, \mathbf{y}^{[k+1]}) + b_k(\mathbf{x}^{[k+1]} - \mathbf{x}^{[k]}) = 0. \quad (49b)$$

Combining the above equations and $\partial \Psi = \partial f + \partial g + \partial C_r$, and further applying Eq. (41a), the following equation holds

$$\lim_{k \rightarrow \infty} \operatorname{dist}(0, \partial \Psi(\mathbf{x}^{[k]}, \mathbf{y}^{[k]})) = \operatorname{dist}(0, \partial \Psi(\mathbf{x}^*, \mathbf{y}^*)) \leq \epsilon.$$

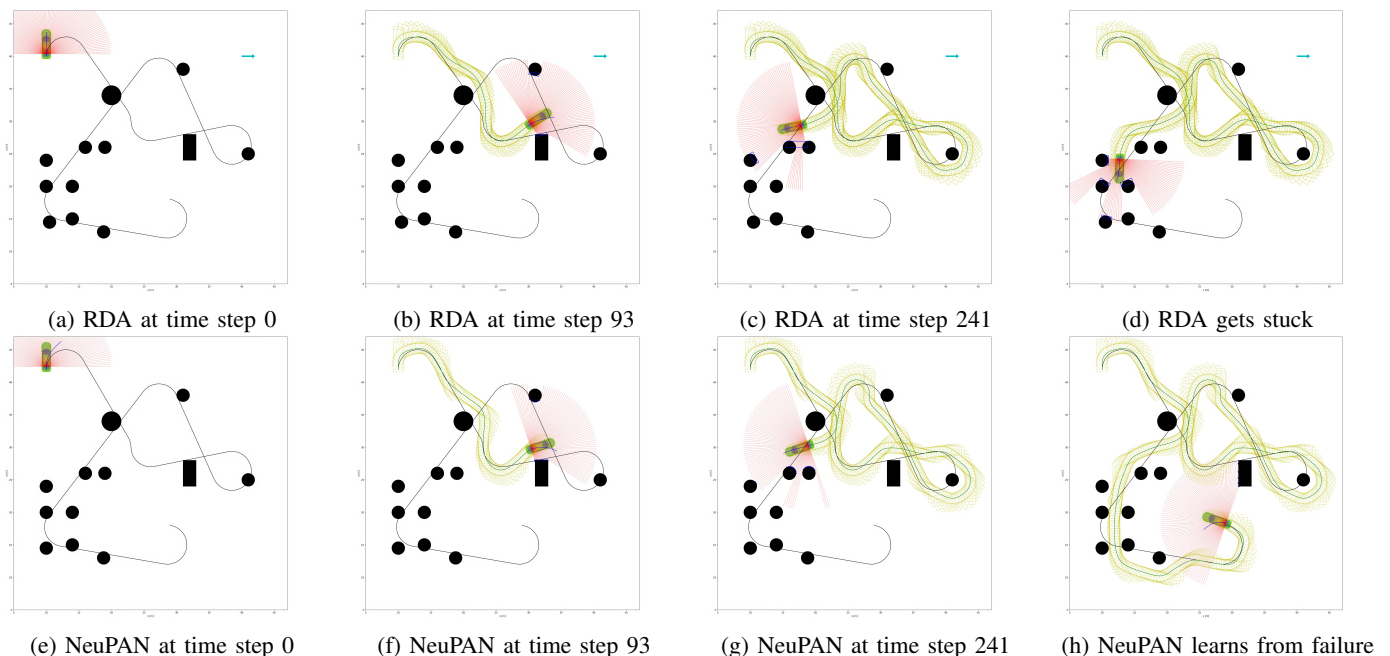


Fig. 21: Navigation process and trajectory comparison of NeuPAN and RDA planner in the path following scenario. The robot is required to plan a trajectory (blue line) to follow the naive path (black line) avoiding the cluttered obstacles (black circle). RDA require the detection algorithm to convert the lidar scan to the convex objects (blue rectangle).

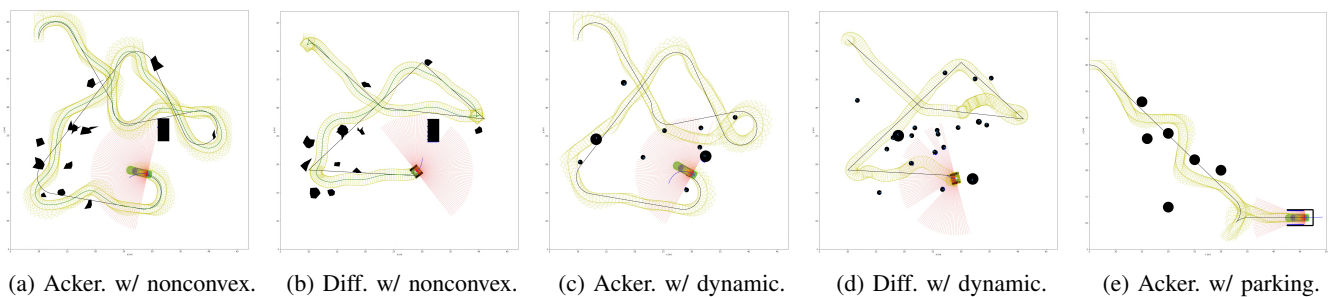


Fig. 22: Verification of NeuPAN in various scenarios on two types of robots.

This proves that every limit point $\{\mathcal{X}^*, \mathcal{Y}^*\}$ of $\{\mathcal{X}^{[k]}, \mathcal{Y}^{[k]}\}$ is a critical point for problem Q. Consequently, to conclude the proof, we only need to show that the sequence converges in finite steps. By leveraging the Kurdyka-Lojasiewicz (KL) property of Ψ and [54][Theorem 1], it can be shown that $\{\mathcal{X}^{[k]}, \mathcal{Y}^{[k]}\}$ is a Cauchy sequence and hence is a convergent sequence approaching the limit $\{\mathcal{X}^*, \mathcal{Y}^*\}$.

APPENDIX D MORE RESULTS BY IR-SIM

This section presents more simulated results in Ir-sim to showcase the effectiveness, efficiency, and trajectory quality of NeuPAN.

A. Path Following

In this scenario, the robot needs to follow a predefined route full of cluttered obstacles, as depicted in Fig. 21 (a). A car-like rectangular robot equipped with a 2D 100-line lidar sensor is considered. The trajectories obtained from the benchmark and the NeuPAN at different frames are shown in Fig. 21(a)-(d) and Fig. 21(e)-(h), respectively. It can be seen that both schemes

are capable of maneuvering the robot in open spaces with sparsely distributed obstacles. However, since the benchmark scheme RDA needs to transform laser scans into boxes or convex sets using object detection (as shown in Fig. 21(c)), errors are inevitably introduced between the detection results and the actual objects. As a consequence, even under ideal lidar and detector in the considered experiment, the modular approach may still result in collisions in densely cluttered environments (as shown in Fig. 21(d)). In contrast, the proposed NeuPAN directly processes the points, thus bypassing intermediate steps, resulting in a more accurate navigation performance in cluttered scenarios.

B. Nonconvex, Dynamic, and Parking Scenarios

To illustrate the comprehensiveness of NeuPAN, we conduct experiments in diverse scenarios using two different robot models: the car-like robot (Ackermann) and the differential-drive robot. The target scenarios and robot trajectories are depicted in Fig. 22. First, Fig. 22(a) and Fig. 22(b) demonstrate the capability of NeuPAN passing through marginal gaps between nonconvex obstacles. To date, nonconvex obstacles

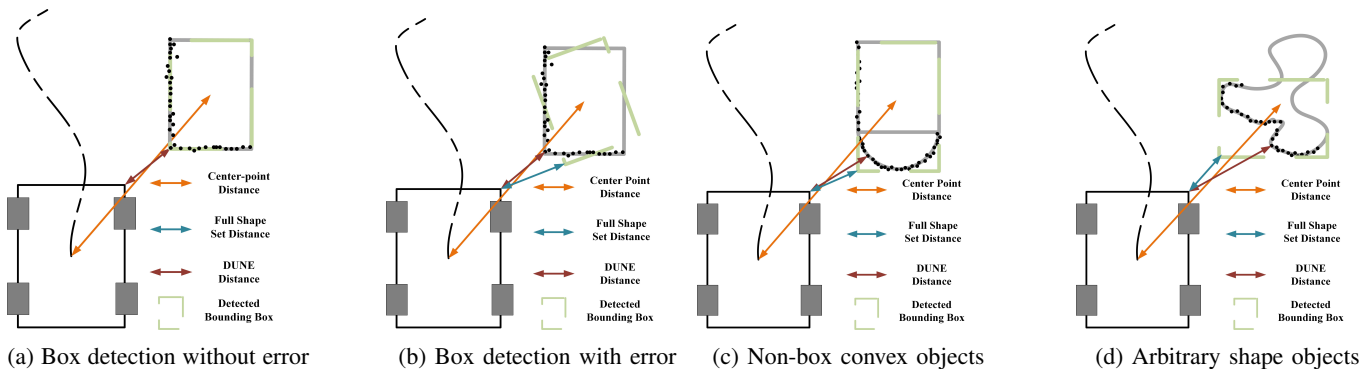


Fig. 23: Intuitive comparison of DUNE distances, center point distances, and full shape set distances. DUNE distances are more accuracy than other distances.

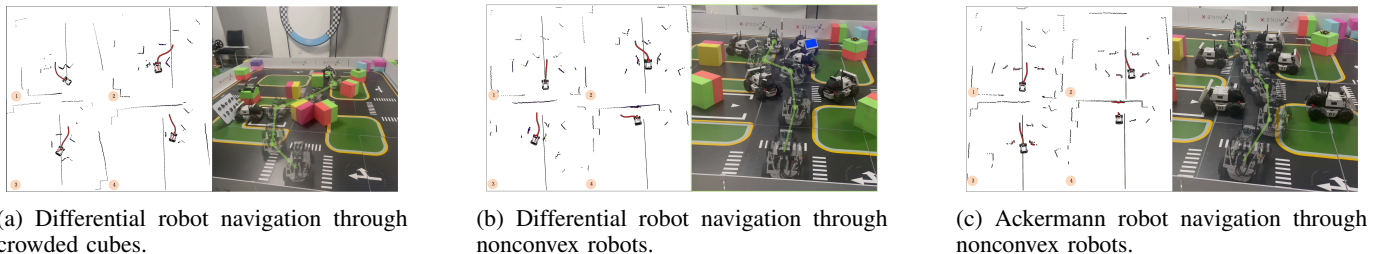


Fig. 24: Navigating differential and Ackermann robots in real world testbed. Red lines are NeuPAN generated trajectories. Black lines are the straight line from the start to end points. Black points are lidar scans.

pose a significant challenge for existing optimization-based approaches [1], [20]. Approximating these nonconvex objects as convex forms would lead to inaccurate representations and dividing them into a group of convex sets would lead to high computation costs. In contrast, the proposed direct point approach efficiently address these complex, nonconvex, and unstructured obstacles. Second, the validation of NeuPAN in dynamic collision avoidance scenarios is illustrated in Figs. 22(c) and 22(d). Finally, the verification of NeuPAN in the reverse parking scenario is presented in Fig. 22(e). These results demonstrate the comprehensiveness and generalizability of our NeuPAN system, which corroborate Table I.

APPENDIX E COMPARISON WITH OTHER DISTANCES

To demonstrate the high-accuracy property of DUNE, we compare the exact distances generated by DUNE and inexact distances generated by other existing approaches. An intuitive comparison is illustrated in Fig. 23. It can be seen that the center point distance has the lowest accuracy, since it does not take the object shape into account. The full shape set distance is accurate if and only if the object has a box shape and the detector is 100% accurate as shown in Fig. 23(a). Otherwise, the set distance would involve non-negligible distance errors as shown in Fig. 23(b) (if the detector is inaccurate) and Fig. 23(c) (if the shape is not a box). Lastly, the proposed DUNE can handle arbitrary nonconvex shapes as shown in Fig. 23(d), whereas all other approaches break down.

APPENDIX F MORE DEMONSTRATIONS IN THE REAL WORLD

To this end, we conduct real-world experiments in a confined testbed to demonstrate the robustness and sim-to-real generalizability of the proposed NeuPAN. The associated results are presented in Fig. 24. The robot is tasked to navigate through a crowd of obstacles to reach the goal point by onboard lidar. Fig. 24(a) shows that the ego-robot under differential steering mode passes the “impassable” area filled with crowded cubes. We have tested solutions including TEB, A-Star, Hybrid A-Star, OBICA, RDA on this challenge and all of them fail. That is why we call it “impassable”. Then, this challenge is further upgraded by replacing the box-shape cubes with nonconvex-shape robots. In such a dense and unstructured geometry, the robot driven by NeuPAN is still able to navigate efficiently, as shown in Fig. 24(b). Finally, we switch the robot mode from differential to Ackermann, which imposes more limitations on robot movements. Under the above change of robot dynamics, most existing learning-based approaches require model retraining. Nonetheless, due to the embedded physical engine in NRMP and the size of the robot does not change, model retraining is not needed for NeuPAN. That is, NeuPAN trained on the differential robot succeeds in directly adapting to the Ackermann robot, as demonstrated in Fig. 24(c). All these experimental results confirm the high-accurate and easy-to-deploy features of NeuPAN in real-world dense (but structured) scenarios.